This is a repository copy of *Structures and Spin States of Iron(II) Complexes of Isomeric 2,6-Di(1,2,3-triazolyl)pyridine Ligands*.

Version: Accepted Version

Article:

Capel Berdiell, I orcid.org/0000-0003-3828-7097, Davies, DJ, Woodworth, J et al. (3 more authors) (2021) Structures and Spin States of Iron(II) Complexes of Isomeric 2,6-Di(1,2,3-triazolyl)pyridine Ligands. Inorganic Chemistry, 60 (19). pp. 14988-15000. ISSN 0020-1669

https://doi.org/10.1021/acs.inorgchem.1c02404

The Structures and Spin States of Iron(II) Complexes of Isomeric 2,6-Di(1,2,3-triazolyl)pyridine Ligands

Izar Capel Berdiell[†,¶], Daniel J. Davies[†], Jack Woodworth[†], Rafal Kulmaczewski[†], Oscar Cespedes[‡], and Malcolm A. Halcrow[†,*]

[†]School of Chemistry, University of Leeds, Woodhouse Lane, Leeds LS2 9JT, UK.

[‡]School of Physics and Astronomy, University of Leeds, E. C. Stoner Building, Leeds LS2 9JT, UK.

*Email address for MAH: m.a.halcrow@leeds.ac.uk.

ABSTRACT: Iron(II) complex salts of 2,6-di(1,2,3-triazol-1-yl)pyridine (L^1) are unexpectedly unstable in undried solvent. This is explained by the isolation of $[Fe(L^1)_4(H_2O)_2][ClO_4]_2$ and $[Fe(NCS)_2(L^1)_2(H_2O)_2]\cdot L^1$, containing L^1 bound as a monodentate ligand rather than in the expected tridentate fashion. These complexes associate into 4^4 grid structures through O–H···N hydrogen bonding; a solvate of a related 4^4 coordination framework *catena*-$[Cu(\mu\text{-}L^1)_2(H_2O)_2][BF_4]_2$ is also presented. The isomeric ligands 2,6-di(1,2,3-triazol-2-yl)pyridine (L^2) and 2,6-di(1*H*-1,2,3-triazol-4-yl)pyridine (L^3) bind to iron(II) in more typical tridentate fashion. Solvates of $[Fe(L^3)_2][ClO_4]_2$ are low-spin and diamagnetic in the solid state and in solution, while $[Fe(L^2)_2][ClO_4]_2$ and $[Co(L^3)_2][BF_4]_2$ are fully high-spin. Treatment of L^3 with methyl iodide affords 2,6-di(2-methyl-1,2,3-triazol-4-yl)pyridine (L^4) and 2-(1-methyl-1,2,3-triazol-4-yl)-6-(2-methyl-1,2,3-triazol-4-yl)pyridine (L^5). While salts of $[Fe(L^5)_2]^{2+}$ are low-spin in the solid state, $[Fe(L^4)_2][ClO_4]_2\cdot H_2O$ is high-spin while $[Fe(L^4)_2][ClO_4]_2\cdot 3MeNO_2$ exhibits a hysteretic spin-transition to 50 % completeness at $T_{½} = 128$ K ($\Delta T_{½} = 6$ K). This transition proceeds *via* a symmetry-breaking phase transition, to an unusual low-temperature phase containing unique three cation sites with high-spin, low-spin and 1:1 mixed-spin populations. The unusual distribution of spin states in the low-temperature phase reflects "spin state frustration" of the mixed spin cation site, by an equal number of high-spin and low-spin nearest neighbors. Gas phase DFT calculations reproduce the spin-state preferences of these and some related complexes. These highlight the interplay between the σ-basicity and π-acidity of the heterocyclic donors in this ligand type, which have opposing influences on the molecular ligand field. The Brønsted basicities of L^1-L^3 are very sensitive to the linkage isomerism of their triazolyl donors, which explains why their iron complex spin states show more variation than the better-known iron(II)/2,6-di(pyrazolyl)pyridine system.

Introduction

Spin-crossover (SCO) compounds continue to be heavily studied, for a number of reasons.[1-3] SCO switches are useful components in switchable fluorescent,[4] conducting,[5] magnetic[6] or dielectric materials,[7,8] and retain their functionality in soft materials[9] and at the mesoscale[10] and nanoscale[11] for device fabrication. More fundamentally, time-resolved switching of SCO compounds has also yielded new insights into the molecular mechanism of crystalline phase changes in the solid state,[12] and of fundamental charge-transfer processes in solution.[13] Two popular classes of SCO complexes are derivatives of the isomeric iron(II)/2,6-di(pyrazolyl)pyridine centers $[Fe(1\text{-bpp})_2]^{2+}$ [14-18] and $[Fe(3\text{-bpp})_2]^{2+}$ [14-16,19,20] (Chart 1). Apart from their synthetic versatility, the SCO temperature of $[Fe(1\text{-bpp})_2]^{2+}$ derivatives can be predictably tuned using appropriate combinations of ligand substituents.[17] Moreover, hydrogen bonding to the N–H groups of $[Fe(3\text{-bpp})_2]^{2+}$ has a strong influence on its spin state which, unusually, makes $[Fe(3\text{-bpp})_2]^{2+}$ stable in aqueous solution.[16,21]

The related 2,6-di(1,2,3-triazolyl)pyridines (b3tp^R, R ≠ H; Scheme 1) ligands are easily prepared by Click chemistry, and are being increasingly employed as metal-binding domains in supramolecular architectures and soft materials.[22] Only a handful of $[Fe(b3tp^R)_2]^{2+}$ complex derivatives have been reported to date, however, which are mostly low-spin in solution and the solid state.[23-26] In contrast, isomeric $[Fe(b4tp^R)_2]^{2+}$ (R = H or Me) complexes are high-spin, with the onset of SCO being detected in one solid complex salt at very low temperature.[27-29] This is a much wider range of spin state properties than observed between analogous $[Fe(1\text{-bpp})_2]^{2+}$ and $[Fe(3\text{-bpp})_2]^{2+}$ derivatives under similar conditions.[16]

To gain insight into this behavior, we report complexes of three isomeric ligands 2,6-di(1,2,3-triazol-1-yl)pyridine (L^1), 2,6-di(1,2,3-triazol-2-yl)pyridine (L^2) and 2,6-di(1*H*-1,2,3-triazol-4-yl)pyridine (L^3 = b3tp^H), which are 1,2,3-triazole-containing analogues of 1-bpp and 3-bpp (Chart 1). While iron(II) compounds are the main focus of this work, a copper(II) complex of L^1 and a cobalt(II) complex of L^3 are also briefly presented. Two dimethylated derivatives L^4 and L^5 are also investigated, including a solvate of $[Fe(L^4)_2][ClO_4]_2$ that undergoes a cooperative, incomplete spin transition coupled to a novel form of crystallographic symmetry breaking.[30] Lastly, we describe DFT calculations addressing why iron complexes of 2,6-di(pyrazolyl)pyridine and 2,6-di(1,2,3-triazolyl)pyridine ligand isomers show such different spin state properties.

Chart 1 Ligands referred to in this work (R = H or alkyl).

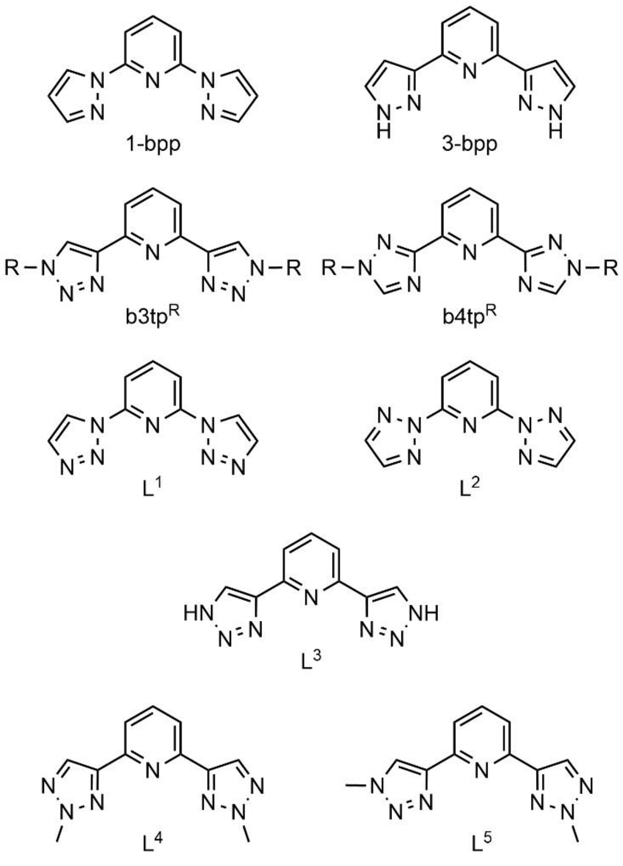

Experimental

Synthetic protocols and characterization data for the new ligands are in the Supporting Information. Other reagents were purchased commercially and used as supplied.

CAUTION Although we have experienced no problem when using the perchlorate salts in this study, metal-organic perchlorates are potentially explosive and should be handled with care in small quantities.

Synthesis of $[\mathrm{Fe(L^1)_4(OH_2)_2}][\mathrm{ClO_4}]_2$ (1[ClO$_4$]$_2$). A mixture of L^1 (0.012 g, 0.056 mmol) and $\mathrm{Fe[ClO_4]_2{\cdot}6H_2O}$ (0.051 g, 0.015 mmol) in MeCN (6 cm^3) was stirred at room temperature until all the solid had dissolved. Slow diffusion of diethyl ether vapor into the filtered, colorless solution afforded colorless crystals of formula **1[ClO$_4$]$_2$**·2MeCN, which decompose to a polycrystalline material upon exposure to air. Yield 0.011 g, 69 %. Elemental analysis for $\mathrm{C_{36}H_{32}Cl_2FeN_{28}O_{10}}$ found (calcd) (%) C, 37.9 (37.8), H, 2.79 (2.82), N, 34.2 (34.3). ESMS *m/z* 241.0460 (calcd for $[\mathrm{Fe(L^1)_2}]^{2+}$ 241.0435), 367.9571 (calcd for $[\mathrm{Fe(L^1)(ClO_4)}]^+$ 367.9592), 385.9686 (calcd for $[\mathrm{Fe(L^1)(OH_2)(ClO_4)}]^+$ 385.9698), 581.0308 (calcd for $[\mathrm{Fe(L^1)_2(ClO_4)}]^+$ 581.0355), 834.8607 (calcd for $[\mathrm{Fe_2(L^1)_2(ClO_4)_3}]^+$ 834.8675), 1303.7667 (calcd for $[\mathrm{Fe_3(L^1)_3(ClO_4)_5}]^+$ 1304.3919).

Synthesis of $[\mathrm{Fe(NCS)_2(L^1)_2(OH_2)_2}]{\cdot}\mathrm{L^1}$ (2·L^1). Method as for **1[ClO$_4$]$_2$**, with the addition of NaNCS (0.003 g, 0.037 mmol) to the colorless metal/ligand solution. This rapidly afforded a dark brown precipitate of unknown composition. Upon standing for some days, the yellow solution also deposited a small number of crystals of **2**·L^1. These were identified crystallographically, but were obtained in too small quantities for analytical characterization.

Synthesis of $[\mathrm{Cu(L^1)_2(OH_2)_2}][\mathrm{BF_4}]_2$ (3[BF$_4$]$_2$). Reaction of L^1 (0.015 g, 0.070 mmol) and $\mathrm{Cu[BF_4]_2{\cdot}6H_2O}$ (0.012 g, 0.035 mmol) in MeCN (8 cm^3) initially afforded a blue suspension, which dissolved upon gentle heating. Blue crystals of the product deposited upon slow cooling of the solution. Yield 0.012 g, 48 %. Elemental analysis for $\mathrm{C_{18}H_{18}B_2CuF_8N_{14}O_2}$ found (calcd) (%) C, 30.8 (30.9), H, 2.49 (2.59), N, 27.9 (28.0). ESMS *m/z* 295.0135 (calcd for $[\mathrm{Cu(L^1)F}]^+$ 295.0037), 508.0806 (calcd for $[\mathrm{Cu(L^1)_2F}]^+$ 508.0800), 576.0842 (calcd for $[\mathrm{Cu(L^1)_2(BF_4)}]^+$ 576.0846), 609.0046 (calcd for $[\mathrm{Cu_2(L^1)_2F_3}]^+$ 609.0064), 677.0058 (calcd for $[\mathrm{Cu_2(L^1)_2F_2(BF_4)}]^+$ 677.0110), 958.0912 (calcd for $[\mathrm{Cu_2(L^1)_3F(BF_4)_2}]^+$ 958.0918).

Synthesis of $[\mathrm{Fe(L^2)_2}][\mathrm{ClO_4}]_2{\cdot}3\mathrm{H_2O}$ (4[ClO$_4$]$_2$·3H$_2$O). $\mathrm{Fe[ClO_4]_2{\cdot}6H_2O}$ (0.019 g, 0.053 mmol) and L^2 (0.022 g, 0.10 mmol) were mixed in nitromethane (9 cm^3), which immediately yielded a yellow solution. Slow diffusion of diethyl ether vapor into the filtered solution afforded yellow crystals of formula **4[ClO$_4$]$_2$**·2MeNO$_2$, which decompose on exposure to air. The dried material analyzes with a trihydrate formulation, where the lattice solvent has been replaced by atmospheric moisture. Yield 0.035 g, 47 %. Elemental analysis for $\mathrm{C_{18}H_{14}Cl_2FeN_{14}O_8{\cdot}3H_2O}$ found (calcd) (%) C, 29.3 (29.4), H, 2.75 (2.74), N, 26.5 (26.7). ES-MS *m/z* 236.0658 (calcd for $[\mathrm{NaL^2}]^+$ 236.0655), 367.9591 (calcd for $[\mathrm{Fe(L^2)(ClO_4)}]^+$ 367.9592), 581.0361 (calcd for $[\mathrm{Fe(L^2)_2(ClO_4)}]^+$ 581.0355). ^{1}H NMR (CD$_3$CN) δ –13.7 (s, 2H, Py *H*^{4}), 57.2 (s, 8H, Tz *H*$^{4/5}$), 69.7 (s, 4H, Py *H*$^{3/5}$).

Synthesis of $[\mathrm{Fe(L^3)_2}][\mathrm{BF_4}]_2$ (5[BF$_4$]$_2$). A mixture of L^3 (0.020 g, 0.094 mmol) and $\mathrm{Fe[BF_4]_2{\cdot}6H_2O}$ (0.016 g, 0.047 mmol) in acetonitrile (10 cm^3) dissolved to give an orange solution. This was filtered, and concentrated to *ca* 50 % of its original volume. Slow diffusion of di-*iso*propyl ether into the solution gave brown platelet crystals. Yield 0.020 g, 64 %. Elemental analysis for $\mathrm{C_{18}H_{14}B_2F_8FeN_{14}}$ found (calcd) (%) C, 33.0 (32.9), H, 2.28 (2.15), N, 29.8 (29.9).

Synthesis of $[\mathrm{Fe(L^3)_2}][\mathrm{ClO_4}]_2$ (5[ClO$_4$]$_2$). Method as for **5[BF$_4$]$_2$**, using $\mathrm{Fe[ClO_4]_2{\cdot}6H_2O}$ (0.017 g, 0.047 mmol). Slow diffusion of di-*iso*propyl ether vapor into the filtered solution gave orange plates of formula **5[ClO$_4$]$_2$**·2MeCN, which dried to a solvent-free powder *in vacuo*. Yield 0.023 g, 73 %. Elemental analysis for $\mathrm{C_{18}H_{14}Cl_2FeN_{14}O_8}$ found (calcd) (%) C, 31.7 (31.7), H, 2.12 (2.07), N, 28.8 (28.5). ESMS *m/z* 241.0460 (calcd for $[\mathrm{Fe(L^3)_2}]^{2+}$ 241.0435), 481.0706 (calcd for $[\mathrm{Fe(L^3)(L^3{-}H)}]^+$ 481.0791), 581.0274 (calcd for $[\mathrm{Fe(L^3)_2(ClO_4)}]^+$ 581.0355). ^{1}H NMR (CD$_3$CN) δ 8.45 (s, 6H, Py *H*$^{3-5}$), 8.66 (s, 4H, Tz *H*^{5}), 13.7 (br s, 4H, Tz N*H*). Recrystallization of **5[ClO$_4$]$_2$** by slow evaporation from aqueous solution afforded brown crystals with a dihydrate formulation, which retain their lattice water upon drying. Elemental analysis for $\mathrm{C_{18}H_{14}Cl_2FeN_{14}O_8{\cdot}2H_2O}$ found (calcd) (%) C, 30.0 (30.1), H, 2.31 (2.53), N, 27.2 (27.3).

Synthesis of $[\mathrm{Co(L^3)_2}][\mathrm{BF_4}]_2$ (6[BF$_4$]$_2$). A mixture of L^3 (0.012 g, 0.056 mmol) and $\mathrm{Co[BF_4]_2{\cdot}6H_2O}$ (0.010 g, 0.028 mmol) in acetone (10 cm^3) gave a pink solution upon stirring at room temperature. Red crystals of the complex were obtained upon slow diffusion of diethyl ether vapor into the filtered solution. Yield 0.010 g, 53 %. Elemental analysis for $C_{18}H_{14}B_2CoF_8N_{14}$ found (calcd) (%) C, 32.9 (32.8), H, 2.25 (2.14), N, 29.6 (29.8). ESMS *m/z* 242.5435 (calcd for $[Co(L^3)_2]^{2+}$ 242.5426), 484.0778 (calcd for $[Co(L^3)(L^3{-}H)]^+$ 484.0774). ^{1}H NMR (CD_3CN) δ 19.7 (s, 2H, Py *H*^{4}), 33.2 (s, 4H, Tz N*H*), 68.5 (s, 4H, Tz *H*^{5}), 93.5 (s, 4H, Py *H*$^{3/5}$).

Synthesis of [Co(L^3)$_2$][ClO$_4$]$_2$ (6[ClO$_4$]$_2$). Method as for **6[BF$_4$]$_2$**, using $Co[ClO_4]_2{\cdot}6H_2O$ (0.014 g, 0.038 mmol). The product was a red crystalline solid. Yield 0.009 g, 42 %. Elemental analysis for $C_{18}H_{14}Cl_2CoN_{14}O_8$ found (calcd) (%) C, 31.4 (31.6), H, 2.12 (2.06), N, 28.5 (28.7).

Synthesis of [Fe(L^4)$_2$][ClO$_4$]$_2$ (7[ClO$_4$]$_2$). Reaction of $Fe[ClO_4]_2{\cdot}6H_2O$ (0.011 g, 0.030 mmol) with L^4 (0.015 g, 0.062 mmol) in nitromethane (7 cm^3) afforded a yellow solution. This was filtered, and two drops of triethyl orthoformate (a dehydrating agent) were added to the filtrate. Slow diffusion of diethyl ether vapor into the solution led to yellow crystals of the product. Yield 0.015 g, 66 %. Elemental analysis for $C_{22}H_{22}Cl_2FeN_{14}O_8$ found (calcd) (%) C, 35.9 (35.8), H, 2.99 (3.01), N, 26.5 (26.6). ^{1}H NMR (CD_3CN) δ –3.3 (s, 12H, C*H*$_3$), 8.2 (s, 2H, Py *H*^{4}), 25.2 (s, 4H, Tz *H*^{5}), 57.1 (s, 4H, *H*$^{3/5}$).

Synthesis of [Fe(L^5)$_2$][BF$_4$]$_2$ (8[BF$_4$]$_2$). Treatment of $Fe[BF_4]_2{\cdot}6H_2O$ (0.013 g, 0.038 mmol) with L^5 (0.018 g, 0.075 mmol) in acetonitrile (5 cm^3) gave an orange solution, which deposited red single crystals upon slow diffusion of diethyl ether vapor. Yield 0.021 g, 77 %. Elemental analysis for $C_{22}H_{22}B_2F_8FeN_{14}$ found (calcd) (%) C, 37.3 (37.1), H, 2.97 (3.11), N, 27.4 (27.5). ES-MS *m/z* 316.0447 (calcd for $[Fe(L^3)F]^+$ 316.0404), 557.1439 (calcd for $[Fe(L^3)_2F]^+$ 557.1480), 625.1469 (calcd for $[Fe(L^5)_2(BF_4)]^+$ 625.1525). ^{1}H NMR (CD_3CN) δ 3.24 (s, 6H, 1-C*H*$_3$), 6.32 (s, 6H, 2-C*H*$_3$), 7.16 (s, 2H, Py *H*^{4}), 10.69 and 13.60 (both s, 2H, 2x Tz *H*^{5}), 16.52 (s, 4H, Py *H*$^{3/5}$).

Synthesis of Fe(L^5)$_2$][ClO$_4$]$_2$ (8[ClO$_4$]$_2$). Method as for **5[BF$_4$]$_2$**, using $Fe[ClO_4]_2{\cdot}6H_2O$ (0.014 g, 0.038 mmol). The product was a red crystalline solid. Yield 0.018 g, 71 %. Elemental analysis for $C_{22}H_{22}Cl_2FeN_{14}O_8$ found (calcd) (%) C, 35.7 (35.8), H, 2.86 (3.01), N, 26.4 (26.6).

Single crystal X-ray structure determinations

Single crystals of the organic ligands were grown from chloroform solution. Slow evaporation of an aqueous solution of **5[ClO$_4$]$_2$** afforded a mixture of prismatic **5[ClO$_4$]$_2$**·2H$_2$O, and a smaller number of needle-like crystals of uncertain composition.[31] Crystals of the other complexes were grown from the following solvent/antisolvent combinations: **1[ClO$_4$]$_2$**·2MeCN, **2**·L^1, **3[BF$_4$]$_2$**·2MeCN and **8[BF$_4$]$_2$**/**8[BF$_4$]$_2$**·*y*MeCN/**8[BF$_4$]$_2$**·H$_2$O·MeCN, acetonitrile/ diethyl ether; **4[ClO$_4$]$_2$**·2MeNO$_2$ and **7[ClO$_4$]$_2$**·3MeNO$_2$/ **7[ClO$_4$]$_2$**·*x*MeNO$_2$, nitromethane/diethyl ether; **5[ClO$_4$]$_2$**·2MeCN, acetonitrile/di-*iso*propyl ether; **6[BF$_4$]$_2$**·H$_2$O and **7[ClO$_4$]$_2$**·H$_2$O, acetone/diethyl ether.

Diffraction data were measured with an Agilent Supernova dual-source diffractometer, using monochromated Cu-K_α (λ = 1.5418 Å) or Mo-K_α (λ = 0.7107 Å) radiation and an Oxford Cryostream cryostat. Experimental details of the structure determinations are listed in Tables S1 and S2. The structures were all solved by direct methods (*SHELXS97*[32]), and developed by full least-squares refinement on F^2 (*SHELXL-2018*[32]). Crystallographic figures were prepared using *XSEED*,[33] and coordination volumes (V_{Oh}) were calculated using *Olex2*.[34] Detailed crystallographic refinement procedures are described in the Supporting Information.

Other measurements

Elemental microanalyses were performed by the microanalytical services at the University of Leeds School of Chemistry, or the London Metropolitan University School of Human Sciences. Electrospray mass spectra were recorded on a Bruker MicroTOF-q instrument from $CHCl_3$ solution. Diamagnetic NMR spectra employed a Bruker AV3HD spectrometer operating at 400.1 (^{1}H) or 100.6 MHz (^{13}C), while paramagnetic ^{1}H NMR spectra were obtained with a Bruker AV3 spectrometer operating at 300.1 MHz. X-ray powder diffraction measurements were obtained at room temperature from a Bruker D2 Phaser diffractometer, using Cu-K_α radiation (λ = 1.5419 Å)

Magnetic susceptibility measurements employed a Quantum Design MPMS-3 VSM magnetometer, in an applied field of 5000 G with a temperature ramp of 5 K min^{-1}. Diamagnetic corrections for the samples were estimated from Pascal's constants;[35] a diamagnetic correction for the sample holder was also applied to the data. Susceptibility measurements in solution were obtained by Evans method using a Bruker AV-NEO spectrometer operating at 500.2 MHz.[36] A diamagnetic correction for the sample,[35] and a correction for the variation of the density of the CD_3CN solvent with temperature,[37] were applied to these data. Thermodynamic parameters and equilibrium midpoint temperatures ($T_{½}$) were derived by fitting these data to eq 1 and 2, where nHS(T) is the high-spin fraction of the sample at temperature T:

$$\ln[(1-n\mathrm{HS}(T))/n\mathrm{HS}(T)] = \Delta H/RT - \Delta S/R \tag{1}$$

$$\Delta S = \Delta H/T_{½} \tag{2}$$

DFT calculations were performed using *SPARTAN'18*,[38] with the B86PW91 functional and def2-SVP basis set. Low spin systems were treated as spin restricted and high spin systems spin unrestricted. The calculations were performed in the gas phase, since a solvent gradient for iron was not implemented in *SPARTAN'18* at the time of writing. Crystallographic atomic coordinates for the complexes were used as a starting point for the geometry minimizations, where available. Otherwise, initial models were constructed from crystallographic coordinates for the high- and low-spin forms of $[Fe(1\text{-bpp})_2]^{2+}$,[39] with ligand C atoms replaced by N atoms as appropriate.

Results and Discussion

Treatment of 2,6-difluoropyridine with 2 equiv of sodium 1,2,3-triazolate in DMF affords L^1 in 57 % yield (Chart 1). The moderate yield reflects competitive electrophilic attack at *N*2 of the triazolate anion during the reaction.[40] Consistent with that, L^2 could also be obtained in *ca.* 10 % yield from chromatographic purifications of these reactions. The unsymmetric derivative 2-(1,2,3-triazol-1-yl)-6-(1,2,3-triazol-2-yl)pyridine was also present in the product mixture, but wasn't isolated in NMR purity. Methylation of L^3 [41] with MeI in the presence of Na_2CO_3 afforded L^4 (33 % yield) and L^5 (14 % yield) after chromatographic separation (Chart 1). Poorly selective alkylation of the triazolyl *N*1 and *N*2 atoms under these conditions is consistent with previous reports.[40] The identities of all the new ligands were confirmed crystallographically (Figures S5-S12).

Reactions of L^1 and $FeX_2\cdot6H_2O$ ($X^- = BF_4^-$ or ClO_4^-) in as-supplied $MeNO_2$ or MeCN, under ambient conditions, initially afford dark orange or yellow solutions implying complex formation. However, the solutions bleach over a period of minutes, sometimes with the formation of a white precipitate. Colorless crystals of *trans*-$[Fe(L^1)_4(OH_2)_2][ClO_4]_2\cdot2MeCN$ (**1[ClO$_4$]$_2$**·2MeCN) could be obtained from the filtered MeCN solutions, upon slow addition of Et_2O antisolvent. The iron centres in this compound coordinate to four monodentate L^1 ligands *via* a triazolyl *N*3 donor atom (Figure 1). This is the usual coordination mode for iron complexes of monodentate 1-alkyl- or 1-aryl-1,2,3-triazoles.[42] A tendency for L^1 to coordinate in monodentate rather than tridentate fashion would explain the hydrolytic instability of its iron complex.

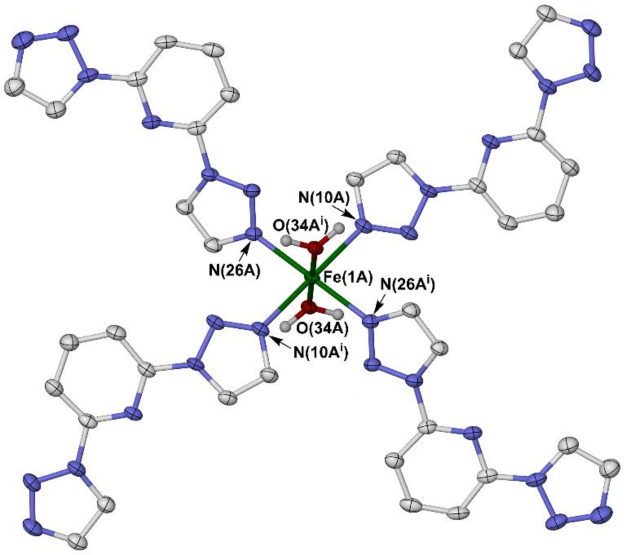

Figure 1 One of the two unique $[Fe(L^1)_4(OH_2)_2]^{2+}$ cations in the crystal structure of **1[ClO$_4$]$_2$**·2MeCN. Atomic displacement ellipsoids are at the 50 % probability level, and C-bound H atoms are omitted for clarity. Symmetry code: (i) 1–*x*, 2–*y*, 1–*z*. Color code C, white; H, grey; Fe, green; N, blue.

Each $[Fe(L^1)_4(OH_2)_2]^{2+}$ cation donates four intermolecular O–H···N hydrogen bonds from its water ligands, to a pendant triazolyl *N*3 atom from four different neighbor molecules. That associates the cations into a 4^4 hydrogen bond network topology, within the (110) crystal plane (Figure S14). Each wall of the grid is formed from two stacked L^1 ligands, which are oriented almost coplanar with the 2D network. Hence the grid cavities are lined with C–H groups, and have approximate dimensions of 3.7 x 8.4 Å. Adjacent cation layers in **1[ClO$_4$]$_2$**·2MeCN are horizontally offset, so the voids within each layer are filled by the vertices of its two neighbors (Figure S15).

Following this result, a covalent 4^4 network structure containing $[Fe(\mu\text{-}L^1)_2X_2]^{n+}$ nodes (X = a monodentate ligand or anion) was sought, which might exhibit SCO when X = NCS^- or $NCSe^-$ for example.[43] However, the only crystalline product obtained of this type was mononuclear *cis*,*trans*,*cis*-$[Fe(NCS)_2(L^1)_2(OH_2)_2]\cdot L^1$ (**2**·L^1), which formed in low yield when NaNCS was added to freshly prepared solutions of **1[ClO$_4$]$_2$**. The complex molecules in **2**·L^1 associate into hydrogen-bonded sheets along the (001) plane, through O–H···N hydrogen bonds between aqua ligands and L^1 triazolyl groups, with the uncoordinated L^1 acting as a linear linker in the hydrogen bond network. However, in contrast to **1[ClO4]$_2$**·2MeCN, the L^1 ligands in **2** associate into stacks along the [100] direction which makes the network in **2** more compact. Hence, although the hydrogen bonding topology of **2**·L^1 is also 4^4, there are no cavities in the 2D network of that compound (Figures S17-S18).

While no coordination networks of L^1 were obtained from iron(II) reagents, a copper(II) framework *catena*-$[Cu(\mu\text{-}L^1)_2(OH_2)_2][BF_4]_2\cdot2MeCN$ (**3[BF$_4$]$_2$**·2MeCN) was prepared with this topology. This compound forms a canted 4^4 grid structure along the $(10\bar{1})$ crystal plane, based on approximately square Cu(II) nodes with axial water ligands. The L^1 ligands are oriented approximately perpendicular to the grid structure, so its cavities are lined by the ligand π-systems. These cavities have approximate dimensions 7.8 x 7.8 Å and are occupied by BF_4^- and MeCN molecules (Figure 2). The grids in the lattice are co-parallel, non-interpenetrating, horizontally offset and linked into three dimensions by O–H···O hydrogen bonding between water ligands (Figure S20). There is no long-range porosity in any of these L^1 complex crystals.

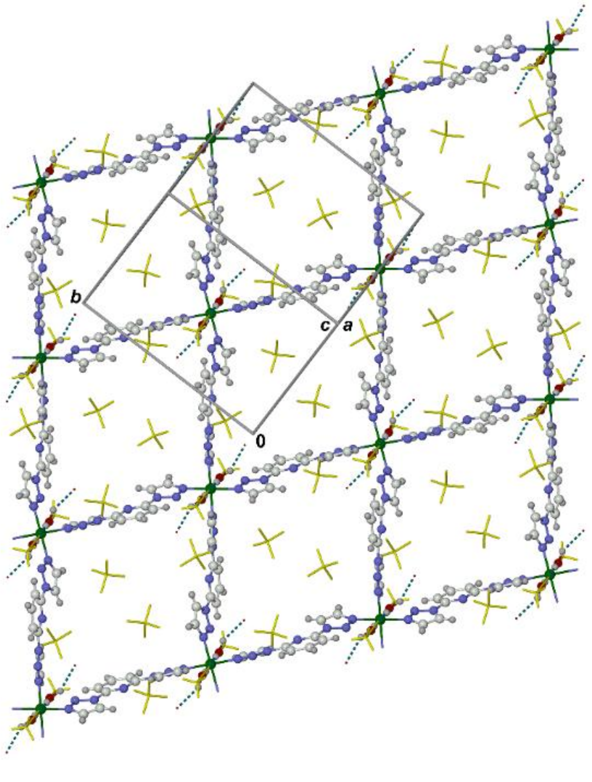

Figure 2 Fragment of the 4^4 network in **3[BF$_4$]$_2$**·2MeCN, showing its unit cell. Color code C {complex}, white; H {complex}, grey; Cu, green; N {complex}, blue; BF_4^- and MeCN, yellow. The view is parallel to the $[10\bar{1}]$ crystal vector.

Although **2**·L^1 was not prepared in sufficient quantity for bulk characterization, **1[ClO$_4$]$_2$** and **3[BF$_4$]$_2$** lose their lattice solvent on drying by microanalysis while retaining their framework structures by powder diffraction (Figure S21). Electrospray mass spectra of **1[ClO$_4$]$_2$** and **3[BF$_4$]$_2$** from MeCN solution contain strong peaks corresponding to $[M(L^1)_2]^{2+}$ and/or $[M(L^1)_2Y]^+$ (M = Fe^{2+} or Cu^{2+}, Y$^-$ = anion) molecular ions, although these putative homoleptic species were not isolated in practise (Figure S22). Both spectra also contain weaker peaks derived from $[M_2(L^1)_2Y_3]^+$, $[M_2(L^1)_3Y_3]^+$ and/or $[M_3(L^1)_3Y_5]^+$ species which indicate partial aggregation of the complexes in solution.

In contrast, L^2-L^5 all form stable complexes with iron(II) salts, where the ligands are bound in the expected tridentate manner. These were characterized as either their BF$_4^-$ or ClO$_4^-$ salts, as in each case only one of these anions yielded useful single crystals. Some of these compounds were investigated in different solvate crystal forms, since lattice solvent can strongly perturb the properties of a solid SCO complex, even in isostructural solvate crystals.[44] However, this is only discussed in detail for one of the following compounds, where different solvates of the same complex salt were indeed found to have distinct spin state properties.

The nitromethane solvate of $[Fe(L^2)_2][ClO_4]_2 \cdot 2MeNO_2$ (**4[ClO$_4$]$_2$**·2MeNO$_2$) was crystallographically characterized, which converts to a hydrate phase **4[ClO$_4$]$_2$**·3H$_2$O upon drying through replacement of its lattice solvent by atmospheric moisture. Crystallographic and magnetic susceptibility data revealed this material is high-spin between 5-300 K (Table 1, Figures S23 and S43). High-spin iron complexes of 1-bpp and 3-bpp derivatives, which might otherwise be expected to exhibit SCO, can adopt distorted coordination geometries which trap them in their high-spin form in the solid state.[14,16] However, the geometry of **4[ClO$_4$]$_2$**·2MeNO$_2$ is sufficiently regular that this is unlikely to contribute to its high-spin nature (Figure S42).

Three forms of $[Fe(L^3)_2][ClO_4]_2$ (**5[ClO$_4$]$_2$**) were obtained: an acetonitrile solvate **5[ClO$_4$]$_2$**·2MeCN; and two hydrated forms which crystallize together upon slow evaporation of aqueous solutions of the compound. The majority form in the hydrate samples has the stoichiometry **5[ClO$_4$]$_2$**·2H$_2$O by microanalysis and powder diffraction (Figure S24). However, this is often contaminated by a second $[Fe(L^3)_2]^{2+}$-containing product, which was crystallographically characterized but whose exact composition is uncertain (Figure S25).[31] All three forms of **5[ClO$_4$]$_2$** contain low-spin $[Fe(L^3)_2]^{2+}$ cations at 120 K (Tables 1 and S13), which is consistent with most other compounds of the $[Fe(b3tp^R)_2]^{2+}$ type.[23-25] The L^3 ligand binds exclusively as its di(1*H*-1,2,3-triazol-4-yl)pyridine tautomer (Chart 1), with extensive hydrogen bonding between the cations, anions and solvent in the lattice.

Magnetic susceptibility data confirmed that **5[ClO$_4$]$_2$**·2H$_2$O and **5[ClO$_4$]$_2$**·2MeCN remain fully low spin at $T \leq 350$ K (Figure S43). In view of this, the cobalt complex $[Co(L^3)_2]^{2+}$ was also examined, since imine-donor ligands that yield low-spin iron(II) complexes may support SCO when bound to cobalt(II).[45,46] This compound was crystallized as its hydrated BF$_4^-$ salt **6[BF$_4$]$_2$**·H$_2$O (tetragonal, $I4_1/a$), which has a complex cation with crystallographic $\bar{4}$ symmetry and extensive

Table 1 Selected metric parameters for representative iron(II) complexes in this study with tridentate heterocyclic ligands (Å, Å^3, °). V_{Oh}, Σ and Θ are indices characteristic for the spin state of a complex, while ϕ and θ relate to structural distortions often found with this tridentate ligand geometry.[47] More detailed bond length and angle Tables are given in Tables S12 and S16-S18.

	4[ClO$_4$]$_2$·2MeNO$_2$	**5[ClO$_4$]$_2$**·2H$_2$O^{a,b}	**7[ClO$_4$]$_2$**·H$_2$O^{a,b}	**7[ClO$_4$]$_2$**·3MeNO$_2$ phase 1^a
Fe–N{pyridyl}	2.134(2), 2.135(2)	1.929(2), 1.931(2)	2.134(2)	2.117(3)
Fe–N{triazolyl}	2.194(2)–2.203(2)	1.940(2)–1.970(2)	2.202(2), 2.224(2)	2.199(2), 2.214(2)
V_{Oh}	12.472(8)	9.608(7)	12.834(7)	12.783(11)
Σ	154.1(3)	85.5(3)	144.8(3)	142.3(10)
Θ	492	277	459	439
ϕ	170.33(8)	178.20(10)	179.57(12)	179.97(15)
θ	88.11(2)	89.86(2)	81.69(2)	86.63(3)

	7[ClO$_4$]$_2$·3MeNO$_2$ phase 2			**8[BF$_4$]$_2$**^{b}
	Molecule A	Molecule B^a	Molecule C^a	
Fe–N{pyridyl}	2.004(5), 2.004(6)	1.918(5)	2.166(6)	1.916(4), 1.925(4)
Fe–N{triazolyl}	2.077(7)–2.096(8)	1.978(7), 1.999(7)	2.223(6), 2.259(7)	1.943(4)–2.013(4)
V_{Oh}	10.98(2)	9.82(2)	13.43(3)	9.624(12)
Σ	118.6(10)	86.2(11)	142.3(10)	86.5(6)
Θ	379	279	452	280
ϕ	179.0(3)	179.8(5)	179.7(5)	176.24(16)
θ	87.88(6)	88.58(5)	87.68(6)	88.34(5)

[a]This molecule has crystallographic C_2 symmetry. [b]Other solvate crystals of these complexes, with similar metric parameters to those here, are also described in the Supporting Information.

disorder of the unique anion and lattice water. However, **6[BF$_4$]$_2$** and **6[ClO$_4$]$_2$** were both high-spin from magnetic susceptibility data, so no SCO was observed (Figures S30 and S43).

The spin-state behavior of solid [Fe(L^4)$_2$][ClO$_4$]$_2$ (**7[ClO$_4$]$_2$**) is more varied. A high-spin monohydrate crystal of this salt was obtained by crystallization from undried acetone (Figure S32). However, recrystallization from MeNO$_2$/Et$_2$O yielded a mixture of solvates: high-spin **7[ClO$_4$]$_2$**·xMeNO$_2$ ($x \approx 0.93$), which has a needle morphology (Figure S35); and, cubic crystals of **7[ClO$_4$]$_2$**·3MeNO$_2$, which undergo an abrupt spin transition upon cooling. While these forms crystallized together, the needle crystals could be removed by decantation to give the SCO-active phase in pure form. Since **7[ClO$_4$]$_2$**·3MeNO$_2$ slowly transforms to **7[ClO$_4$]$_2$**·H$_2$O upon standing in air for 1-2 hrs by powder diffraction (Figure S45), its magnetic measurements were performed using freshly isolated crystals protected under saturated Et$_2$O vapor.

SCO in **7[ClO$_4$]$_2$**·3MeNO$_2$ occurs abruptly to 50 % completeness with narrow thermal hysteresis, at $T_{½}\downarrow$ = 125 and $T_{½}\uparrow$ = 131 K (Figure 3). A crystallographic symmetry- breaking is associated with this spin-transition. At 180 K, phase 1 of the crystal (space group $P2/c$, $Z = 2$) contains one unique high-spin half-molecule of the complex, with crystallographic C_2 symmetry (Figure S33). At 120 K the crystal has transformed to phase 2 ($P2$, $Z = 4$) whose asymmetric unit includes one whole molecule of the complex, plus two unique C_2 symmetric half-molecules (Figure S34). The phase 1→phase 2 transition does not simply reflect loss of the crystallographic c glide, but involves reorientation of the unit cell within the (010) plane (Figure S37). Metric parameters imply whole molecule A in phase 2 is a disordered mixture of high- and low-spin molecules at 120 K, while half-molecule B is low-spin and half-molecule C is high-spin (Table 1). This affords an approximate 1:1 population of high- and low-spin molecules in the crystal, as predicted by the magnetic data. The phase 1/phase 2 transformation occurs concurrently with the magnetochemical spin transition, at 125±5 K in cooling mode and at 135±5 K in warming mode (Figure S44).

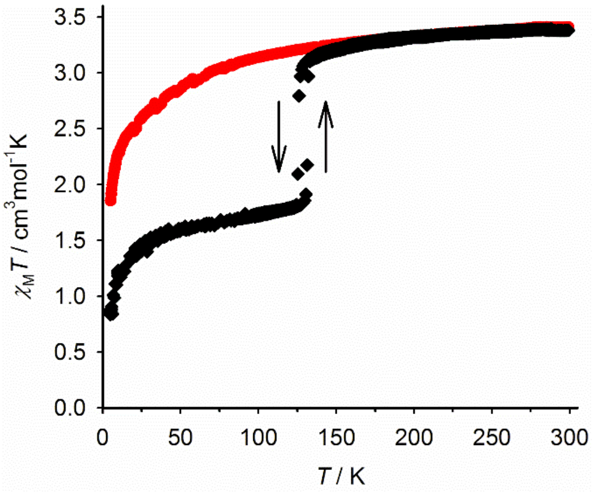

Figure 3 Variable temperature magnetic susceptibility data for **7[ClO$_4$]$_2$**·3MeNO$_2$ (black) and **7[ClO$_4$]$_2$**·H$_2$O (red). Data were measured in cooling and warming modes, at 5 K min^{-1} scan rate.

The spin state distribution in phase 2 can be visualized from its molecular packing in the (010) plane, where the cations are arranged in puckered layers. Each cation has four nearest neighbor cations within its layer, while adjacent layers are separated by anions and solvent (Figure S36). While low-spin molecule B and high-spin molecule C are both surrounded by four 'A' sites in their layer, the mixed-spin cation A site has two low-spin and two high-spin nearest neighbors, in an arrangement that breaks the local C_2 symmetry at that lattice point (Figure 4). SCO is propagated through a material by changes in the local pressure exerted at each lattice site, as the spin-state population evolves in each region of the lattice.[48] Thus, the intermediate lattice pressure exerted on molecule A by two high-spin and two low-spin nearest neighbors, could frustrate the spin state of cation A into a 1:1 high:low-spin population.

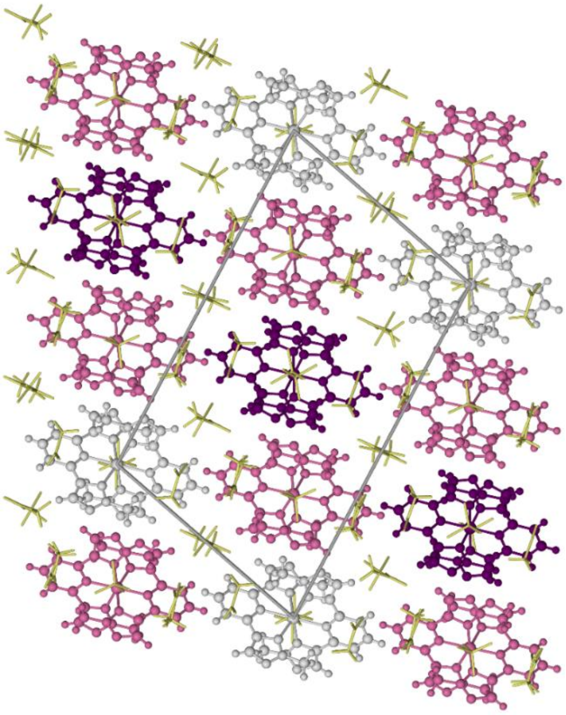

Figure 4 Packing diagram of phase 2 of **7[ClO$_4$]$_2$**·3MeNO$_2$, viewed perpendicular to the (010) crystal plane. The high-spin (white), low-spin (purple) and mixed-spin (pink) molecules in the lattice are highlighted, while anions and solvent (yellow) are de-emphasized for clarity.

There are two noteworthy interactions between the cations in phase 1 (Figure S38). First, is a short face-to-face $\pi\cdots\pi$ contact between triazolyl rings of two cations, across a crystallographic inversion center. The overlapping rings are coplanar by symmetry, and separated by 3.240(11) Å. Second are anion$\cdots\pi$ interactions to a ClO$_4^-$ ion, which is encapsulated by four triazolyl rings from two cations related by translation along a. While the $\pi\cdots\pi$ interactions are retained, some anion$\cdots\pi$ contacts are lost in phase 2 because those anions are now crystallographically ordered. We propose these intermolecular contacts are responsible for propagation of the cooperative spin-transition through the lattice in **7[ClO$_4$]$_2$**·3MeNO$_2$. The disposition of these intermolecular contacts in phase 2 also leads to the spin state frustration of molecule A, as described above.

Finally, $[Fe(L^5)_2][BF_4]_2$ (**8[BF$_4$]$_2$**) formed better crystals than the corresponding perchlorate salt, so this complex was characterized in that form. Three forms of **8[BF$_4$]$_2$** co-crystallized from MeCN/Et_2O mixtures: the solvent-free compound, and two MeCN solvates (Figures S39-S41). All these were low-spin at 120 K by crystallography. The Fe–N bond lengths to the L^5 2-methyltriazolyl donor groups are 0.027(6)-0.068(6) Å longer than to the 1-methyltriazolyl donors, reflecting the steric influence of the distal 2-methyl substituents on the metal coordination sphere (Table S20). This has no wider impact on the structure of the complex, however, which is a typical low-spin molecule of this type. A bulk sample of **8[BF$_4$]$_2$** from the same solvent mixture was a mixture of phases by powder diffraction, and was fully low-spin from magnetic measurements (Figures S43 and S46). Hence, phase-pure samples of **8[BF$_4$]$_2$** for more detailed characterization were not pursued further.

The spin states of **4[ClO$_4$]$_2$-8[BF$_4$]$_2$** in CD_3CN solution were determined by Evans method. This is a better measure of the ligand field experienced by each complex, in the absence of lattice effects that also influence their spin states in the solid state.[49] They showed that **4[ClO$_4$]$_2$**, **6[BF$_4$]$_2$** and **7[ClO$_4$]$_2$** are all fully high-spin over the liquid range of that solvent; **5[ClO$_4$]$_2$** is fully low-spin; and **8[BF$_4$]$_2$** undergoes a spin-state equilibrium with $T_{½} = 342$ K and $\Delta H = 21.8(3)$ kJ mol^{-1} (Figure 5).[50] While the results for the latter compound contrast with its low-spin nature in the solid state, the stability of the high-spin state of **5[ClO$_4$]$_2$** < **8[BF$_4$]$_2$** < **7[ClO$_4$]$_2$** mirrors the number of 2-methyltriazolyl substituents in each compound. Distal methyl substituents in complexes of related tridentate ligands exert a steric influence on the metal coordination sphere, which disfavors the low-spin state.[51,52]

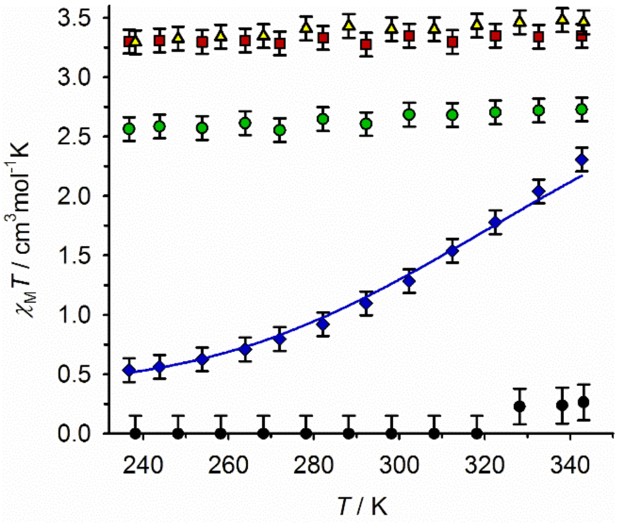

Figure 5 Solution phase magnetic susceptibility data for **4[ClO$_4$]$_2$** (yellow triangles), **5[ClO$_4$]$_2$** (black circles), **6[BF$_4$]$_2$** (green circles), **7[ClO$_4$]$_2$** (red squares) and **8[BF$_4$]$_2$** (blue diamonds) in CD_3CN solution. The line shows the best fit of the data for **8[BF$_4$]$_2$** to eq 1 and 2.[50]

Isomeric L^1-L^3 form iron(II) complexes with very different stabilities and spin state behavior; and, methylation of the triazolyl *N*2 positions in L^3 progressively stabilizes the high-spin state in $[Fe(L^4)_2]^{2+}$ and $[Fe(L^5)_2]^{2+}$. Gas phase DFT calculations of these and some related molecules (Chart 2) were undertaken to explore these results. The calculations employed the B86PW91 functional and def2-SVP basis set, which we have used to probe the effects of ligand geometry on metal ion spin state.[53-55] They are the closest analogues in *SPARTAN'18*[39] of the BP86/def2-SVP functional/basis set combination, which performed well in studies of comparative spin state energies in $[Fe(bpp)_2]^{2+}$ derivatives[17] and other iron(II) compounds.[17,56] The energies of the corresponding free ligands were also minimized by the same protocol, in conformations consistent with tridentate metal coordination (Table S21, Figure S49).[57]

Chart 2 Additional ligands included in the computational study. L$^{3'}$, the unmethylated analogue of L^4, is a tautomer of L^3 (Chart 1).

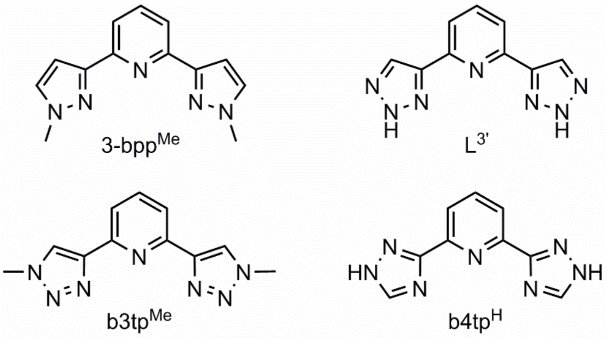

The geometries of the complexes were minimized in their low-spin and high-spin states. The computed and crystallographic low-spin Fe–N bond lengths lie within experimental error, except for $[Fe(L^4)_2]^{2+}$ where the discrepancy is up to 5 crystallographic esds (Table S23). That suggests the steric influence of the L^4 methyl groups might be imperfectly modelled by this functional, which does not account for dispersion interactions between non-bonded atoms.[58] The computed high-spin Fe–N distances are up to 2.5 % longer than the experimental values, but are still within reasonable agreement for a calculation of this type. While the biggest apparent discrepancy is for high-spin $[Fe(3\text{-}bpp^{Me})_2]^{2+}$, the experimental values for that compound are complicated by crystallographic disorder.[52]

The calculated energies of the low- and high-spin states of these complexes are listed in Table 2. Since GGA functionals like B86PW91 overstabilize the low-spin state,[59] the relative stabilities of the spin states ΔE_{rel}(HS–LS) are scaled relative to $[Fe(1\text{-}bpp)_2]^{2+}$, which undergoes SCO in solution at $T_{½} = 248$ K.[40] A positive value of ΔE_{rel}(HS–LS) means a molecule's low-spin state is more stabilized than in $[Fe(1\text{-}bpp)_2]^{2+}$, and *vice versa*. The comparative ΔE_{rel}(HS–LS) values reproduce the solution-phase spin state trends in these compounds well (Figure 6).

Table 2 Computed energies of the high-spin (HS) and low-spin (LS) states of iron(II) complexes of the ligands in Charts 1 and 2. Experimental solution-phase SCO $T_{1/2}$ data are also included, where available.

		$T_{1/2}$ / K	E(HS) / Ha	E(LS) / Ha	ΔE_{rel}(HS–LS) / kcal mol^{-1}
1	$[\mathrm{Fe}(1\text{-bpp})_2]^{2+}$	248[a]	−2659.474752[a]	−2659.500527[a]	0
2	$[\mathrm{Fe}(3\text{-bpp})_2]^{2+}$	247[b]	−2659.522601	−2659.548142	−0.2
3	$[\mathrm{Fe}(3\text{-bpp}^{\mathrm{Me}})_2]^{2+}$	HS[c]	−2816.714724	−2816.730311	−6.4
4	$[\mathrm{Fe}(\mathrm{L}^1)_2]^{2+}$	–	−2723.509188	−2723.547458	+7.8
5	$[\mathrm{Fe}(\mathrm{L}^2)_2]^{2+}$	HS[c]	−2723.528232	−2723.550877	−2.0
6	$[\mathrm{Fe}(\mathrm{L}^3)_2]^{2+}$	LS[d]	−2723.593076	−2723.631224	+7.8
7	$[\mathrm{Fe}(\mathrm{L}^{3'})_2]^{2+}$	–	−2723.552709	−2723.577149	−0.8
8	$[\mathrm{Fe}(\mathrm{L}^4)_2]^{2+}$	HS[c]	−2880.761382	−2880.779386	−4.9
9	$[\mathrm{Fe}(\mathrm{L}^5)_2]^{2+}$	342	−2880.781287	−2880.810482	+2.2
10	$[\mathrm{Fe}(\mathrm{b3tp}^{\mathrm{Me}})_2]^{2+}$	LS[d]	−2880.796513	−2880.833878	+7.3
11	$[\mathrm{Fe}(\mathrm{b4tp}^{\mathrm{H}})_2]^{2+}$	<180[e]	−2723.683544	−2723.705047	−2.7

[a]Data from refs 40 and 53. [b]$T_{1/2}$ of this compound is solvent-dependent. The value quoted is observed in weakly interacting organic solvents (ref. 21). [c]Fully high-spin in solution (ref. 52 or this work). [d]Fully low-spin in solution (ref. 23 or this work). [e]Ref. 27.

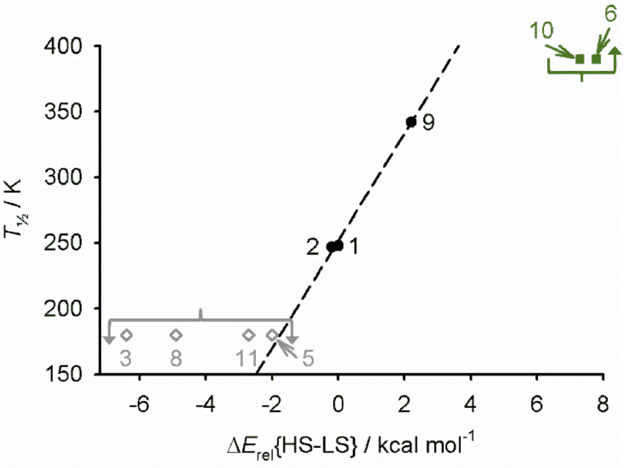

Figure 6 Correlation between measured solution $T_{1/2}$ values and the computed spin state energies in Table 2. Each data point is identified by the corresponding entry in the Table, and the line shows the best fit linear regression of the black data points. Compounds showing SCO near room temperature are black circles; low-spin compounds ($T_{1/2}$ > 350 K) are green squares, and high-spin compounds ($T_{1/2}$ < 180 K) are white diamonds.

There is mostly good agreement between the complex spin states and the Brønsted basicity of the metal-free ligands (Table S22). Thus, the most basic ligands in this study, L^3 and $\mathrm{b3tp}^{\mathrm{Me}}$, form the most strongly low-spin complexes; and, two of the least basic ligands, L^2 and $\mathrm{L}^{3'}$, form complexes computed to be high-spin. It's not possible to quantify the contributions of the individual heterocyclic N-donors to this correlation, because there is extensive mixing of the N lone pair MOs (Figures S51-S56). However, the average energy of the three coordinating lone pair MOs in most of the ligands correlates reasonably with the spin state energies of its iron complex (Figure 7). The scatter in this correlation should reflect the influence of Fe–L π-bonding to the spin state energies, as a smaller perturbation to the Fe←L σ-bonding trend in this series of compounds.[17]

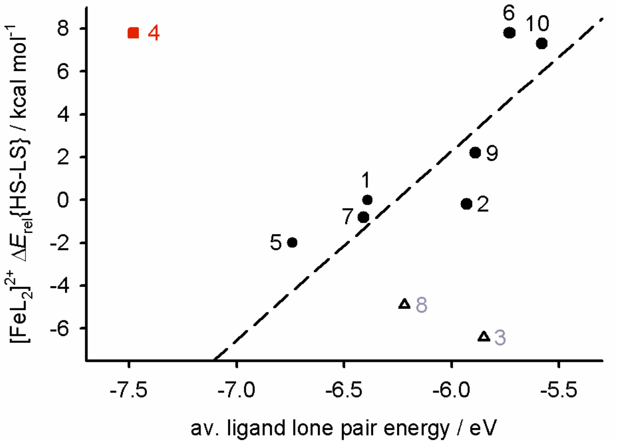

Figure 7 Correlation between the computed spin state energies of the di(1,2,3-triazolyl)pyridine complexes (Table 2), and the average energy of the three coordinating lone pair MOs in the corresponding free ligands (Table S22). The outlier data points are $[\mathrm{Fe}(\mathrm{L}^1)_2]^{2+}$ (red square); and $[\mathrm{Fe}(3\text{-bpp}^{\mathrm{Me}})_2]^{2+}$ and $[\mathrm{Fe}(\mathrm{L}^4)_2]^{2+}$ (white triangles). Other details as for Figure 6.

Three molecules are particular outliers to the trend in Figure 7. Two of them are the complexes bearing four distal methyl substituents, $[\mathrm{Fe}(3\text{-bpp}^{\mathrm{Me}})_2]^{2+}$ and $[\mathrm{Fe}(\mathrm{L}^4)_2]^{2+}$, which are more high-spin than expected from their ligand basicity. That should reflect destabilization of their low-spin state by the steric influence of those methyl groups. Evidently four distal methyl groups are required to influence the complexes' spin states, since ΔE_{rel}(HS–LS) for $[\mathrm{Fe}(\mathrm{L}^5)_2]^{2+}$ follows the same trend as the unsubstituted molecules. The other outlier is $[\mathrm{Fe}(\mathrm{L}^1)_2]^{2+}$, which is discussed further below.

By the average lone pair MO energy measure, ligands with C–C bonds between their pyridyl and azolyl groups (3-bpp, L^3-L^5 and their methylated derivatives, plus $\mathrm{b4tp}^{\mathrm{H}}$) are mostly more basic than ligands whose heterocycles are linked by C–N bonds (1-bpp, L^1 and L^2; Table S22). For example, the average lone pair MO energy of 1-bpp is 0.46 eV lower in energy than for its isomer 3-bpp. That could reflect the impact of two electronwithdrawing N-azolyl substituents adjacent to the pyridyl N-donor atom, in lowering the energy of that lone pair. The inductive effect of C−C/C−N linkage isomerism on the azolyl N-donor basicities should be smaller, since the orientation of the pyrid-2-yl substituents with respect to the azolyl donors is the same in each case.

The substitution pattern of 1,2,3-triazoles has another influence on the basicity of L^1-L^5, in that the basic pK_a of 2-substituted 1,2,3-triazoles is 4-6 units lower than for 1- or 4-substituted triazoles.[60] That contributes to the weak ligand field exerted by L^2 and the tautomer $L^{3'}$, which is the least basic of the "C−C linked" ligands.[57] Thus, $[Fe(L^{3'})_2]^{2+}$ is computed to be 8.6 kcal mol^{-1} more high-spin than $[Fe(L^3)_2]^{2+}$ itself, reflecting the reduced basicity of the 2*H*-triazolyl N-donors in $L^{3'}$, compared to the 1*H*-triazolyl N-donors in L^3 (Table 2).[60] Finally, the "C−N linked" ligands have a narrower ligand bite angle,[61] which should further stabilize their high-spin forms.[53,62] That aspect wasn't quantified in this study, however.

Two aspects of Table 2 cannot be explained by these simple pK_a arguments. First, SCO in the $[Fe(bpp)_2]^{2+}$ isomers occurs at essentially the same temperature in organic solvents, although 1-bpp is computed to be a significantly weaker Brønsted base than 3-bpp (Figure 7). The frontier orbital energies of the ligands and their complexes show 1-bpp is a better π-acid than in 3-bpp, as well as being a weaker σ-base (Figure S50). The stronger π-back-donation and weaker σ-donation in $[Fe(1\text{-}bpp)_2]^{2+}$ have opposite influences on its ligand field,[17] which counterbalance each other almost perfectly (Figure S58). That explains why $[Fe(1\text{-}bpp)_2]^{2+}$ and $[Fe(3\text{-}bpp)_2]^{2+}$ exhibit identical $T_{½}$ values in solution. Similar π-bonding considerations also apply to $[Fe(L^2)_2]^{2+}$ and $[Fe(L^3)_2]^{2+}$ for example, but only as a perturbation to the much larger differences in their Fe−L σ-bonding mentioned above (Figure 7).

The second apparent anomaly is that $[Fe(L^1)_2]^{2+}$ is computed to be low-spin with a similar ΔE_{rel}(HS−LS) to $[Fe(L^3)_2]^{2+}$, despite L^1 being the weakest Brønsted base in this study for tridentate coordination (Table S22). Its *d*-orbital energies show this again arises from its strong metal−ligand σ-bonding, particularly the Fe−N{triazolyl} bonds in the molecular *xy* plane (Figure S61). Evidently, forcing L^1 to adopt tridentate coordination *in silico* causes significant rehybridization of its triazolyl donors.

The experimental preference of L^1 for monodentate coordination reflects that its triazolyl *N*2 lone pairs, which are required for metal chelation, are very low in energy. Rather, the HOMO and HOMO−1 of L^1 are its divergent triazolyl *N*3 lone pair combinations, which are oriented for monodentate coordination of L^1 as observed in **1**-**3** (Figure S53). In practice, the computed low-spin state of tridentate $[Fe(L^1)_2]^{2+}$ would make it a thermodynamic sink in mixtures of iron(II) salts and L^1. Since solutions of that metal and ligand are labile and hydrolytically sensitive, we conclude $[Fe(L^1)_2]^{2+}$ does not exist under the conditions employed in this work. Hence, the $[Fe(L^1)_2ClO_4]^+$ and $[Fe(L^1)_2]^{2+}$ molecular ions detected by mass spectrometry from **1[ClO$_4$]$_2$** might only be stable in the gas phase (Figure S22).

Conclusion

Iron(II) complexes of the regioisomeric 2,6-di(1,2,3-triazolyl)pyridine ligands L^1-L^3 show more variable coordination and spin state properties than their better-known pyrazolyl analogues, 1-bpp and 3-bpp (Chart 1). L^1 acts exclusively as a monodentate or *bis*-monodentate ligand in this work, binding metals through its triazolyl *N*3 donor atoms. That reflects that these are the most basic N-donors in that molecule, according to gas phase DFT calculations. Thus, it resembles its analogue 2,6-di(1,2,4-triazol-1-yl)pyridine, which also forms coordination polymers through *bis*-monodentate coordination.[63] Since L^1 can form covalent coordination polymers under the correct conditions (Figure 2), it has potential as a basic or exogenous metal binding linear linker in functional framework materials.[64]

The other ligands in this study bind metal ions in the expected tridentate fashion. Unexpectedly, the spin state properties of $[Fe(L^2)_2]^{2+}$ and $[Fe(L^3)_2]^{2+}$ show much greater variation than the comparable isomeric pair $[Fe(1\text{-}bpp)_2]^{2+}$ and $[Fe(3\text{-}bpp)_2]^{2+}$. DFT calculations rationalize this from the large difference in Brønsted basicity between the triazol-4-yl N-donor groups in L^3 and the triazol-2-yl donors in L^2, which differ by around 6 pK_a units.[58] This is the main factor controlling the different spin states of their iron complexes (Figure 7). In contrast, the basic pK_as of the pyrazol-1-yl donor groups in 1-bpp and the pyrazol-3-yl donors in 3-bpp should be more similar, at within around 1-2 units of each other.[65] These pK_a predictions are confirmed by the computed lone pair orbital energies for each ligand (Table S22).

Another contributor to the spin states of the complexes is the significantly different electronic character of pyridyl donors bound to two *N*-azolyl or *C*-azolyl substituents. The lower σ-basicity and greater π-acidity of the 2,6-di(*N*-azolyl)pyridyl moiety have opposing effects on a metal's ligand field. These offset each other almost perfectly in $[Fe(1\text{-}bpp)_2]^{2+}$ and $[Fe(3\text{-}bpp)_2]^{2+}$, giving those molecules almost identical spin state properties (Figure S58). However, the larger variation in the σ-basicity of the triazole donors dominates the properties of those complexes. That explains the different spin state characteristics of the bpp and L^1-L^3 ligand series.

Sequential methylation of the distal *N*2 atoms in $[Fe(L^4)_2]^{2+}$ and $[Fe(L^5)_2]^{2+}$ progressively stabilizes their high-spin states (Table 2). That trend has an electronic as well as a steric origin, because of the relative lone pair energies of *N*1 *vs* *N*2-alkylated triazoles (Figure S52).[60] As a result, thermal SCO was observed in a solvate salt of $[Fe(L^4)_2]^{2+}$, **7[ClO$_4$]$_2$**·3MeNO$_2$. This spin-transition occurs abruptly with a narrow thermal hysteresis, to only 50 % completeness (Figure 3). The crystal undergoes a crystallographic phase-change during the transition, to a low-temperature phase containing a 1:1 high:low-spin state population distributed between three unique lattice sites (Figure 4).

Cooperative spin-transitions are often associated with crystallographic phase transitions, which can lead to complex multi-phase behavior.[30,66,67] However, incomplete SCO involving symmetry breaking from a spin-pure to a mixed-spin phase is less common.[66] Moreover this is the first example of this form of symmetry-breaking in an SCO material, giving a 1:1 high:low-spin population distributed across three unique crystallographic sites.

ASSOCIATED CONTENT

Supporting Information.

NMR spectra for the organic ligand and complexes; experimental data, refinement procedures and tabulated metric parameters for the crystal structure determinations; X-ray powder diffraction and additional solid state magnetic susceptibility data; details of the minimized structures from the DFT calculations, and frontier orbital plots (PDF).

Accession Codes

CCDC 2099823–2099829, 2099835–2099844 and 2099869 contain the supplementary crystallographic data for this paper. These data can be obtained free of charge via www.ccdc.cam.ac.uk/data_request/cif, or by emailing data_request@ccdc.cam.ac.uk, or by contacting The Cambridge Crystallographic Data Centre, 12 Union Road, Cambridge CB2 1EZ, UK; fax: +44 1223 336033.

Data Sets

Experimental data sets associated with this paper are available from the University of Leeds library (http://doi.org/10.5518/1042).

AUTHOR INFORMATION

Present Address

¶ Centre for Materials Science and Nanotechnology, University of Oslo, P.O Box 1126, Blindern, 0318 Oslo, Norway.

Author Contributions

All authors have given approval to the final version of the manuscript.

Notes

The authors declare no competing financial interests.

ACKNOWLEDGMENT

The authors thank Simon Barrett (University of Leeds) for the solution phase magnetic measurements. This work was funded by the Leverhulme Trust (RPG-2015-095), the EPSRC (EP/K012576/1), the Royal Society of Chemistry (Undergraduate Research Bursary to JW) and the University of Leeds.

REFERENCES

(1) Gütlich, P.; Goodwin, H. A. (eds.) *Spin Crossover in Transition Metal Compounds I–III, Topics in Current Chemistry*; Springer-Verlag: Berlin, 2004; Vols. 233–235.

(2) Halcrow, M. A. (ed), *Spin-Crossover Materials - Properties and Applications,* John Wiley & Sons, Ltd.: New York, 2013, p. 568.

(3) For recent general reviews of SCO complexes see: (a) Brooker, S. Spin Crossover with Thermal Hysteresis: Practicalities and Lessons Learnt. *Chem. Soc. Rev.* **2015**, *44*, 2880–2892. (b) Sato, O. Dynamic Molecular Crystals with Switchable Physical Properties. *Nature Chem.* **2016**, *8*, 644–656. (c) Kumar, K. S.; Ruben, M. Emerging Trends in Spin Crossover (SCO) Based Functional Materials and Devices. *Coord. Chem. Rev.* **2017**, *346*, 176–205. (d) Yao, Z.-S.; Tang, Z.; Tao, J. Bistable Molecular Materials with Dynamic Structures. *Chem. Commun.* **2020**, *56*, 2071–2086.

(4) See eg (a) Wang, C.-F.; Li, R.-F.; Chen, X.-Y.; Wei, R.-J.; Zheng, L.-S.; Tao, J. Synergetic Spin Crossover and Fluorescence in One-Dimensional Hybrid Complexes. *Angew. Chem., Int. Ed.* **2015**, *54*, 1574–1577. (b) Lochenie, C.; Schötz, K.; Panzer, F.; Kurz, H.; Maier, B.; Puchtler, F.; Agarwal, S.; Köhler, A.; Weber, B. Spin-Crossover Iron(II) Coordination Polymer with Fluorescent Properties: Correlation between Emission Properties and Spin State. *J. Am. Chem. Soc.* **2018**, *140*, 700−709. (c) Delgado, T.; Meneses-Sánchez, M.; Piñeiro-López, L.; Bartual-Murgui, C.; Muñoz, M. C.; Real, J. A. Thermo- and Photo-Modulation of Exciplex Fluorescence in a 3D Spin Crossover Hofmann-Type Coordination Polymer. *Chem. Sci.* **2018**, *9*, 8446–8452. (d) Benaicha, B.; Van Do, K.; Yangui, A.; Pittala, N.; Lusson, A.; Sy, M.; Bouchez, G.; Fourati, H.; Gómez-García, C. J.; Triki, S.; Boukheddaden, K. Interplay Between Spin-Crossover and Luminescence in a Multifunctional Single Crystal Iron(II) Complex: Towards a New Generation of Molecular Sensors. *Chem. Sci.* **2019**, *10*, 6791–6798. (e) Ge, J.-Y.; Chen, Z.; Zhang, L.; Liang, X.; Su, J.; Kurmoo, M.; Zuo, J.-L. A Two-Dimensional Iron(II) Coordination Polymer with Synergetic Spin-Crossover and Luminescent Properties. *Angew. Chem. Int. Ed.* **2019**, *58*, 8789–8793. (f) Lathion, T.; Fürstenberg, A.; Besnard, C.; Hauser, A.; Bousseksou, A.; Piguet, C. Monitoring Fe(II) Spin-State Equilibria via Eu(III) Luminescence in Molecular Complexes: Dream or Reality? *Inorg. Chem.* **2020**, *59*, 1091−1103.

(5) Wang, M.; Li, Z.-Y.; Ishikawa, R.; Yamashita, M. Spin Crossover and Valence Tautomerism Conductors. *Coord. Chem. Rev.* **2021**, *435*, 213819.

(6) See eg (a) Ababei, R.; Pichon, C.; Roubeau, O.; Li, Y.-G.; Bréfuel, N.; Buisson, L.; Guionneau, P.; Mathonière, C.; Clérac, R. Rational Design of a Photomagnetic Chain: Bridging Single-Molecule Magnets with a Spin-Crossover Complex. *J. Am. Chem. Soc.* **2013**, *135*, 14840–14853. (b) Feng, X.; Mathonière, C.; Jeon, I.-R.; Rouzières, M.; Ozarowski, A.; Aubrey, M. L.; Gonzalez, M. I.; Clérac, R.; Long, J. R. Tristability in a Light-Actuated Single-Molecule Magnet. *J. Am. Chem. Soc.* **2013**, *135*, 15880–15884. (c) Urtizberea, A.; Roubeau, O. Switchable Slow Relaxation of Magnetization in the Native Low Temperature Phase of a Cooperative Spin-Crossover Compound. *Chem. Sci.* **2017**, *8*, 2290–2295. (d) Darawsh, M.; Barrios, L. A.; Roubeau, O.; Teat, A. J.; Aromí, G. Encapsulation of a CrIII Single-Ion Magnet within an FeII Spin-Crossover Supramolecular Host. *Angew. Chem. Int. Ed.* **2018**, *57*, 13509–13513. (e) Rabelo, R.; Toma, L.; Moliner, N.; Julve, M.; Lloret, F.; Pasán, J.; Ruiz-Pérez, C.; Ruiz-García, R.; Cano, J. Electroswitching of the Single-Molecule Magnet Behaviour in an Octahedral Spin Crossover Cobalt(II) Complex with a Redox-Active Pyridinediimine Ligand. *Chem. Commun.* **2020**, *56*, 12242–12245.

(7) See eg. (a) Zhang, X.; Mu, S.; Chastanet, G.; Daro, N.; Palamarciuc, T.; Rosa, P.; Létard, J.-F.; Liu, J.; Sterbinsky, G. E.; Arena, D. A.; Etrillard, C.; Kundys, B.; Doudin, B.; Dowben, P. A. Complexities in the Molecular Spin Crossover Transition. *J. Phys. Chem. C* **2015**, *119*, 16293–16302. (b) Bovo, G.; Bräunlich, I.; Caseri, W. R.; Stingelin, N.; Anthopoulos, T. D.; Sandeman, K. G.; Bradley, D. D. C.; Stavrinou, P. N. Room Temperature Dielectric Bistability in Solution-Processed Spin Crossover Polymer Thin Films. *J. Mater. Chem. C* **2016**, *4*, 6240–6248. (c) Rat, S.; Piedrahita-Bello, M.; Salmon, L.; Molnár, G.; Demont, P.; Bousseksou, A. Coupling Mechanical and Electrical Properties in Spin Crossover Polymer Composites. *Adv. Mater.* **2018**, *30*, 1705275. (d) Zheng, H.; Meng, Y.-S.; Zhou, G.-L.; Duan, C.-Y.; Sato, O.; Hayami, S.; Luo, Y.; Liu, T. Simultaneous Modulation of Magnetic and Dielectric Transition via Spin-Crossover-Tuned Spin Arrangement and Charge Distribution. *Angew. Chem. Int. Ed.* **2018**, *57*, 8468 –8472. (e) Soroceanu, I.; Graur, A.; Coca, E.; Salmon, L.; Molnár, G.; Demont, P.; Bousseksou, A.; Rotaru, A. Broad-Band Dielectric Spectroscopy Reveals Peak Values of Conductivity and Permittivity Switching upon Spin Crossover. *J. Phys. Chem. Lett.* **2019**, *10*, 7391−7396.

(8) (a) Jornet-Mollá, V.; Duan, Y.; Giménez-Saiz, C.; Tang, Y.-Y.; Li, P.-F.; Romero, F. M.; Xiong, R.-G. A Ferroelectric Iron(II) Spin Crossover Material. *Angew. Chem. Int. Ed.* **2017**, *56*, 14052–14056. (b) Akiyoshi, R.; Hirota, Y.; Kosumi, S.; Tsutsumi, M.; Nakamura, M.; Lindoy, L. F.; Hayami, S. Ferroelectric Metallomesogens Composed of Achiral Spin Crossover Molecules. *Chem. Sci.* **2019**, *10*, 5843–5848.

(9) (a) Gaspar, A. B.; Seredyuk, M. Spin Crossover in Soft Matter. *Coord. Chem. Rev.* **2014**, *268*, 41–58. (b) Kuroiwa, K. Supramolecular

Control of Spin Crossover Phenomena Using Various Amphiphiles. *Inorganics* **2017**, *5*, 45. (c) Enriquez-Cabrera, A.; Rapakousiou, A.; Piedrahita Bello, M.; Molnár, G.; Salmon, L.; Bousseksou, A. Spin Crossover Polymer Composites, Polymers and Related Soft Materials. *Coord. Chem. Rev* **2020**, *419*, 213396.

(10) Manrique-Juárez, M. D.; Rat, S.; Salmon, L.; Molnár, G.; Quintero, C. M.; Nicu, L.; Shepherd, H. J.; Bousseksou, A. Switchable Molecule-Based Materials for Micro- and Nanoscale Actuating Applications: Achievements and Prospects. *Coord. Chem. Rev.* **2016**, *308*, 395–408.

(11) (a) Molnár, G.; Rat, S.; Salmon, L.; Nicolazzi, W.; Bousseksou, A. Spin Crossover Nanomaterials: From Fundamental Concepts to Devices. *Adv. Mater.* **2018**, *30*, 1703862. (b) Coronado, E. Molecular Magnetism: from Chemical Design to Spin Control in Molecules, Materials and Devices. *Nature Rev. Mater.* **2020**, *5*, 87−104.

(12) (a) Bertoni, R.; Lorenc, M.; Tissot, A.; Boillot, M.-L.; Collet, E. Femtosecond Photoswitching Dynamics and Microsecond Thermal Conversion Driven by Laser Heating in Fe^{III} Spin-Crossover Solids. *Coord. Chem. Rev.* **2015**, *282–283*, 66–76. (b) Chergui, M.; Collet, E. Photoinduced Structural Dynamics of Molecular Systems Mapped by Time-Resolved X‑ray Methods. *Chem. Rev.* **2017**, *117*, 11025–11065.

(13) Zhang, W.; Gaffney, K. J. Mechanistic Studies of Photoinduced Spin Crossover and Electron Transfer in Inorganic Complexes. *Acc. Chem. Res.* **2015**, *48*, 1140–1148.

(14) Halcrow, M. A. Iron(II) Complexes of 2,6-Di(pyrazol-1-yl)pyridines – a Versatile System for Spin-Crossover Research. *Coord. Chem. Rev.* **2009**, *253*, 2493–2514.

(15) Olguín, J.; Brooker, S. Spin Crossover Active Iron(II) Complexes of Selected Pyrazole-Pyridine/Pyrazine Ligands. *Coord. Chem. Rev.* **2011**, *255*, 203–240.

(16) Kershaw Cook, L. J.; Mohammed, R.; Sherborne, G.; Roberts, T. D.; Alvarez, S.; Halcrow, M. A. Spin State Behaviour of Iron(II)/Dipyrazolylpyridine Complexes. New Insights from Crystallographic and Solution Measurements. *Coord. Chem. Rev.* **2015**, *289–290*, 2–12.

(17) Kershaw Cook, L. J.; Kulmaczewski, R.; Mohammed, R.; Dudley, S.; Barrett, S. A.; Little, M. A.; Deeth, R. J.; Halcrow, M. A. A Unified Treatment of the Relationship Between Ligand Substituents and Spin State in a Family of Iron(II) Complexes. *Angew. Chem. Int. Ed.* **2016**, *55*, 4327–4331.

(18) Selected recent examples of [Fe(1-bpp)$_2$]$^{2+}$ derivatives: (a) Kumar, K. S.; Šalitroš, I.; Boubegtiten-Fezoua, Z.; Moldovan, S.; Hellwig, P.; Ruben, M. A Spin Crossover (SCO) Active Graphene-Iron(II) Complex Hybrid Material. *Dalton Trans.* **2018**, *47*, 35–40. (b) Douib, H.; Cornet, L.; Flores Gonzalez, J.; Trzop, E.; Dorcet, V.; Gouasmia, A.; Ouahab, L.; Cador, O.; Pointillart, F. Spin-Crossover and Field-Induced Single-Molecule Magnet Behaviour in Metal(II)-Dipyrazolylpyridine Complexes. *Eur. J. Inorg. Chem.* **2018**, *2018*, 4452–4457. (c) Attwood, M.; Akutsu, H.; Martin, L.; Cruickshank, D.; Turner, S. S. Above Room Temperature Spin Crossover in Thioamide-Functionalised 2,6-Bis(pyrazol-1-yl)pyridine Iron(II) Complexes. *Dalton Trans.* **2019**, *48*, 90–98. (d) Kumar, K. S.; Heinrich, B.; Vela, S.; Moreno-Pineda, E.; Bailly, C.; Ruben, M. Bi-stable Spin-Crossover Characteristics of a Highly Distorted [Fe(1-BPP-COOC$_2$H$_5$)$_2$](ClO$_4$)$_2$·CH$_3$CN Complex. D*alton Trans.* **2019**, *48*, 3825–3830. (e) Kumar, K. S.; Del Giudice, N.; Heinrich, B.; Douce, L.; Ruben, M. Bistable Spin-Crossover in a New Series of [Fe(BPP-R)$_2$]$^{2+}$ (BPP = 2,6-Bis(pyrazol-1-yl)pyridine; R = CN) Complexes. *Dalton Trans.* **2020**, *49*, 14258–14267. (f) Palacios-Corella, M.; Ramos-Soriano, J.; Souto, M.; Ananias, D.; Calbo, J.; Ortí, E.; Illescas, B.M.; Clemente-Leon, M.; Martín, N.; Coronado, E. Hexakis-Adducts of [60]Fullerene as Molecular Scaffolds of Polynuclear Spin-Crossover Molecules. *Chem. Sci.* **2021**, *12*, 757–766. (g) Kulmaczewski, R.; Bamiduro, F.; Shahid, N.; Cespedes, O.; Halcrow, M. A. Structural Transformations and Spin-Crossover in [FeL$_2$]$^{2+}$ Salts (L=4-{*tert*-Butylsulfanyl}-2,6-di{pyrazol-1-yl}pyridine): the Influence of Bulky Ligand Substituents. *Chem. Eur. J.* **2021**, *27*, 2082–2092. (h) Galadzhun, I.; Kulmaczewski, R.; Shahid, N.; Cespedes, O.; Howard, M. J.; Halcrow, M. A. The Flexibility of Long Chain Substituents Influences Spin-Crossover in Isomorphous Lipid Bilayer Crystals. *Chem. Commun.* **2021**, *57*, 4039–4042.

(19) Craig, G. A.; Roubeau, O.; Aromí, G. Spin State Switching in 2,6-Bis(pyrazol-3-yl)pyridine (3-bpp) Based Fe(II) Complexes. C*oord. Chem. Rev.* **2014**, *269*, 13–31.

(20) Selected recent examples of [Fe(3-bpp)$_2$]$^{2+}$ derivatives: (a) Giménez-López, M. C.; Clemente-León, M.; Giménez-Saiz, C. Unravelling the Spin-State of Solvated [Fe(bpp)$_2$]$^{2+}$ Spin-Crossover Complexes: Structure–Function Relationship. *Dalton Trans.* **2018**, *47*, 10453–10462. (b) Djemel, A.; Stefanczyk, O.; Marchivie, M.; Trzop, E.; Collet, E.; Desplanches, C.; Delimi, R.; Chastanet, G. Solvatomorphism-Induced 45 K Hysteresis Width in a Spin-Crossover Mononuclear Compound. *Chem. Eur. J.* **2018**, *24*, 14760–14767. (c) Nikovskiy, I.; Polezhaev, A.; Novikov, V.; Aleshin, D.; Pavlov, A.; Saffiulina, E.; Aysin, R.; Dorovatovskii, P.; Nodaraki, L.; Tuna, F.; Nelyubina. Yu. Towards the Molecular Design of Spin-Crossover Complexes of 2,6-Bis(pyrazol-3-yl)pyridines. *Chem. Eur. J.* **2020**, *26*, 5629–5638. (d) Jornet-Mollá, V.; Giménez-Saiz, C.; Yufit, D. S.; Howard, J. A. K.; Romero, F. M. A Reversible Hydrogen-Bond Isomerization Triggered by an Abrupt Spin Crossover near Room Temperature. *Chem. Eur. J.* **2021**, *27*, 740−750. (e) Jornet-Mollá, V.; Giménez-Saiz, C.; Cañadillas-Delgado, L.; Yufit, D. S.; Howard, J. A. K.; Romero, F. M. Interplay Between Spin Crossover and Proton Migration Along Short Strong Hydrogen Bond. *Chem. Sci.* **2021**, *12*, 1038–1053. (f) Benmansour, S.; Gómez-Claramunt, P.; Gómez-García, C. J. Effects of Water Removal on the Structure and Spin-Crossover in an Anilato-Based Compound. *J. Appl. Phys.* **2021**, *129*, 123904. (g) Djemel, A.; Stefanczyk, O.; Desplanches, C.; Kumar, K.; Delimi, R.; Benaceur, F.; Ohkoshi, S.; Chastanet, G. Switching on Thermal and Light-Induced Spin Crossover by Desolvation of [Fe(3-bpp)$_2$](XO$_4$)$_2$·solvent (X = Cl, Re) Compounds. *Inorg. Chem. Front.* **2021**, *8*, 3210–3221. (h) Üngör, Ö.; Choi, E. S.; Shatruk, M. Optimization of Crystal Packing in Semiconducting Spin-Crossover Materials with Fractionally Charged TCNQ$^{\delta-}$ Anions ($0 < \delta < 1$). *Chem. Sci.* **2021**, *12*, 10765–10779.

(21) (a) Barrett, S. A.; Kilner, C. A.; Halcrow, M. A. Spin-Crossover in [Fe(3-bpp)$_2$][BF$_4$]$_2$ in Different Solvents – a Dramatic Stabilisation of the Low-Spin State in Water. *Dalton Trans.* **2011**, *40*, 12021–12024. (b) Jeon, I.-R.; Park, J. G.; Haney, C. R.; Harris, T. D. Spin Crossover Iron(II) Complexes as PARACEST MRI Thermometers. *Chem. Sci.* **2014**, *5*, 2461–2465.

(22) (a) Byrne, J. P.; Kitchen, J. A.; Gunnlaugsson, T. The btp [2,6-Bis(1,2,3-triazol-4-yl)pyridine] Binding Motif: a New Versatile Terdentate Ligand for Supramolecular and Coordination Chemistry. *Chem. Soc. Rev.* **2014**, *43*, 5302–5325. (b) van Hilst, Q. V. C.; Lagesse, N. R.; Preston, D.; Crowley, J. D. Functional Metal Complexes from CuAAC "Click" Bidentate and Tridentate Pyridyl-1,2,3-Triazole Ligands. *Dalton Trans.* **2018**, *47*, 997–1002.

(23) Li, Y.; Huffman, J. C.; Flood, A. H. Can Terdentate 2,6-Bis(1,2,3-Triazol-4-yl)pyridines Form Stable Coordination Compounds? *Chem. Commun.* **2007**, *2007*, 2692–2694.

(24) (a) Meudtner, R. M.; Ostermeier, M.; Goddard, R.; Limberg, C.; Hecht, S. Multifunctional "Clickates" as Versatile Extended Heteroaromatic Building Blocks: Efficient Synthesis via Click Chemistry, Conformational Preferences, and Metal Coordination. *Chem. Eur. J.* **2007**, *13*, 9834–9840. (b) Ostermeier, M.; Berlin, M.-A.; Meudtner, R. M.; Demeshko, S.; Meyer, F.; Limberg, C.; Hecht, S. Complexes of Click-Derived Bistriazolylpyridines: Remarkable Electronic Influence of Remote Substituents on Thermodynamic Stability as well as Electronic and Magnetic Properties. *Chem. Eur. J.* **2010**, *16*, 10202–10213. Some [Fe(b3tp^{R})$_2$]$^{2+}$ derivatives in this study exhibit thermal SCO at accessible temperatures. That can be attributed to the electronic influence of their alkoxy pyridyl ligand substituents, which should stabilize their high-spin state.[17]

(25) Dierks, P.; Kruse, A.; Bokareva, O. S.; Al-Marri, M. J.; Kalmbach, J.; Baltrun, M.; Neuba, A.; Schoch, R.; Hohloch, S.; Heinze, K.; Seitz, M.; Kühn, O.; Lochbrunner S.; Bauer, M. Distinct

Photodynamics of κ-N and κ-C Pseudoisomeric Iron(II) Complexes. *Chem. Commun.* **2021**, *57*, 6640–6643.

(26) Iron-containing metallopolymers with metal-binding b3tp^{R} residues in their backbone or side-chain have also been reported. (a) Meudtner, R. M.; Hecht, S. Responsive Backbones Based on Alternating Triazole-Pyridine/Benzene Copolymers: From Helically Folding Polymers to Metallosupramolecularly Crosslinked Gels. *Macromol. Rapid Commun.* **2008**, *29*, 347–351. (b) Munuera, L.; O'Reilly, R. K. Using Metal–Ligand Interactions for the Synthesis of Metallostar Polymers. *Dalton Trans.* **2010**, *39*, 388–391.

(27) Sugiyarto, K. H.; Craig, D. C.; Rae, A. D.; Goodwin, H. A. Structural and Electronic Properties of Iron(II) and Nickel(II) Complexes of 2,6-Bis(triazol-3-yl)pyridines. *Aust. J. Chem.* **1993**, *46*, 1269–1290.

(28) Renz, F.; De Souza, P. A.; Klingelhöfer, G.; Goodwin, H. A. Molecular Sensors for Moisture Detection by Mössbauer Spectroscopy. *Hyperfine Interact.* **2002**, *139–140*, 699–704.

(29) Scudder, M. L.; Craig, D. C.; Goodwin, H. A. Hydrogen Bonding Influences on the Properties of Heavily Hydrated Chloride Salts of Iron(II) and Ruthenium(II) Complexes of 2,6-Bis(pyrazol-3-yl)pyridine, 2,6-Bis(1,2,4-triazol-3-yl)pyridine and 2,2':6',2''-terpyridine. *CrystEngComm* **2005**, *7*, 642–649.

(30) (a) Shatruk, M.; Phan, H.; Chrisostomo, B. A.; Suleimenova, A. Symmetry-Breaking Structural Phase Transitions in Spin Crossover Complexes. *Coord. Chem. Rev.* **2015**, *289–290*, 62–73. (b) Ortega-Villar, N.; Muñoz, M. C.; Real, J. A. Symmetry Breaking in Iron(II) Spin-Crossover Molecular Crystals. *Magnetochemistry* **2016**, *2*, 16.

(31) The byproduct co-crystallizing with **5[ClO$_4$]$_2$**·2H$_2$O contains a low-spin $[\mathrm{Fe(L^3)_2}]^{2+}$ cation, three apparent water half-molecules on crystallographic special positions, and just one $\mathrm{ClO_4^-}$ anion per asymmetric unit. It's unclear whether the crystal has a mixed $\mathrm{ClO_4^-/X^-}$ ($\mathrm{X^-}$ = a monoatomic anion) formulation, or if it contains a deprotonated $[\mathrm{L^3}]^-$ ligand which would also lead to charge balance (Figure S25).

(32) Sheldrick, G. M. A Short History of *SHELX*. *Acta Cryst. Sect. A Found. Cryst.* **2008**, *64*, 112−122.

(33) Barbour, L. J. *X-Seed* – A Software Tool for Supramolecular Crystallography. *J. Supramol. Chem.* **2001**, *1*, 189−191.

(34) Dolomanov, O. V.; Bourhis, L. J.; Gildea, R. J.; Howard, J. A. K.; Puschmann, H. *OLEX2*: a Complete Structure Solution, Refinement and Analysis Program. *J. Appl. Cryst.* **2009**, *42*, 339−341.

(35) O'Connor, C. J. Magnetochemistry – Advances in Theory and Experimentation. *Prog. Inorg. Chem.* **1982**, *29*, 203−283.

(36) (a) Evans, D. F. The Determination of the Paramagnetic Susceptibility of Substances in Solution by Nuclear Magnetic Resonance. *J. Chem. Soc.* **1959**, 2003–2005. (b) Schubert, E. M. Utilizing the Evans Method with a Superconducting NMR Spectrometer in the Undergraduate Laboratory. *J. Chem. Educ.* **1992**, *69*, 62.

(37) García, B.; Ortega, J. C. Excess Viscosity η^{E}, Excess Volume V^{E}, and Excess Free Energy of Activation ΔG^{*E} at 283, 293, 303, 313, and 323 K for Mixtures of Acetonitrile and Alkyl Benzoates. *J. Chem. Eng. Data* **1988**, *33*, 200−204**.**

(38) *Spartan'16*, Wavefunction Inc., Irvine CA, USA, **2016**.

(39) Holland, J. M.; McAllister, J. A.; Kilner, C. A.; Thornton-Pett, M.; Bridgeman, A. J.; Halcrow, M. A. Stereochemical Effects on the Spin-State Transition Shown by Salts of $[\mathrm{FeL_2}]^{2+}$ [L = 2,6-Di(pyrazol-1-yl)pyridine]. *J. Chem. Soc. Dalton Trans.* **2002**, 548–554.

(40) Wang, X.-J.; Zhang, L.; Krishnamurthy, D.; Senanayake, C. H.; Wipf, P. General Solution to the Synthesis of *N*-2-Substituted 1,2,3-Triazoles. *Org. Lett.* **2010**, *12*, 4632–4635.

(41) Thomas, J.; Jana, S.; Liekens, S.; Dehaen, W. A Single-Step Acid Catalyzed Reaction for Rapid Assembly of *NH*-1,2,3-Triazoles. *Chem. Commun.* **2016**, *52*, 9236−9239.

(42) Aromí, G.; Barrios, L. A.; Roubeau, O.; Gamez, P. Triazoles and Tetrazoles: Prime Ligands to Generate Remarkable Coordination Materials. *Coord. Chem. Rev.* **2011**, *255*, 485–546.

(43) Sciortino, N. F.; Neville, S. M. Two-Dimensional Coordination Polymers with Spin Crossover Functionality. *Aust. J. Chem.* **2014**, *67*, 1553–1562.

(44) See *eg* (a) Hostettler, M.; Törnroos, K. W.; Chernyshov, D.; Vangdal, B.; Bürgi, H.-B. Challenges in Engineering Spin Crossover: Structures and Magnetic Properties of Six Alcohol Solvates of Iron(II) Tris(2-picolylamine) Dichloride. *Angew. Chem. Int. Ed.* **2004**, *43*, 4589–4594. (b) Wei, R.-J.; Tao, J.; Huang, R.-B.; Zheng, L.-S. Reversible and Irreversible Vapor-Induced Guest Molecule Exchange in Spin-Crossover Compounds. *Inorg. Chem.* **2011**, *50*, 8553–8564. (c) Kershaw Cook, L. J.; Kulmaczewski, R.; Cespedes, O.; Halcrow, M. A. Different Spin-State Behaviors in Isostructural Solvates of a Molecular Iron(II) Complex. *Chem. Eur. J.* **2016**, *22*, 1789–1799. (d) Phonsri, W.; Harding, P.; Liu, L.; Telfer, S. G.; Murray, K. S.; Moubaraki, B.; M. Ross, T. M.; Jameson, G. N. L.; Harding, D. J. Solvent Modified Spin Crossover in an Iron(III) Complex: Phase Changes and an Exceptionally Wide Hysteresis. *Chem. Sci.* **2017**, *8*, 3949–3959.

(45) Barefield, E. K.; Busch, D. H.; Nelson, S. M. Iron, Cobalt, and Nickel Complexes Having Anomalous Magnetic Moments. *Q. Rev. Chem. Soc.* **1968**, *22*, 457−498.

(46) (a) Goodwin, H. A. Spin Crossover in Cobalt(II) Systems. *Top. Curr. Chem.* **2004**, *234*, 23–47. (b) Krivokapic, I.; Zerara, M.; Daku, M L.; Vargas, A.; Enachescu, C.; Ambrus, C.; Tregenna-Piggott, P.; Amstutz, N.; Krausz, E.; Hauser, A. Spin-crossover in cobalt(II) imine complexes. *Coord. Chem. Rev.* **2007**, *251*, 364–378. (c) Hayami, S.; Komatsu, Y.; Shimizu, T.; Kamihata, H.; Lee, Y. H. Spin-Crossover in Cobalt(II) Compounds Containing Terpyridine and its Derivatives. *Coord. Chem. Rev.* **2011**, *255*, 1981–1990.

(47) V_{Oh} is the volume of the octahedron defined by the $\mathrm{FeN_6}$ coordination sphere.[68] Σ is a general measure of the deviation of a metal ion from an ideal octahedral geometry, while Θ more specifically indicates its distortion towards a trigonal prismatic structure. Σ and Θ are usually much larger in the high-spin than in the low-spin state; a perfectly octahedral complex gives $\Sigma = \Theta = 0$.[68,69] ϕ is the *trans*-N{pyridyl}–Fe–N{pyridyl} bond angle, while θ is the dihedral angle between the least squares planes of the two tridentate ligands. An undistorted D_{2d}-symmetric complex of this type will give $\phi = 180°$ and $\theta = 90°$.[14,16] More detailed definitions of these parameters are in the cited references, and in the Supporting Information to this article.

(48) Enachescu, C.; Nicolazzi, W. Elastic Models, Lattice Dynamics and Finite Size Effects in Molecular Spin Crossover Systems. *C. R. Chimie* **2018**, *21*, 1179−1195.

(49) Guionneau, P.; Marchivie, M.; Chastanet, G. Multiscale Approach of Spin Crossover Materials: A Concept Mixing Russian Dolls and Domino Effects. *Chem. Eur. J.* **2021**, *27*, 1483–1486.

(50) Solution phase magnetic data for **8[BF$_4$]$_2$** could only be fit to eq 1 and 2 after correcting for a constant 0.35 $\mathrm{cm^3\,mol^{-1}\,K}$ paramagnetic impurity, corresponding to a 10 % residual high-spin iron(II) fraction. This may reflect some ligand dissociation from the complex, which is visible by ^{1}H NMR in the associating $\mathrm{CD_3CN}$ solvent (Figure S48), and is slow on the timescale of the SCO equilibrium. Hassan, N.; Koudriavtsev, A. B.; Linert, W. Isoequilibrium Relationships and Cooperative Effects in Spin-State Transitions in Solution. *Pure Appl. Chem.* **2008**, *80*, 1281−1292.

(51) Baker, A. T.; Goodwin, H. A. Iron(II) and Nickel(II) Complexes of 2,6-Di(thiazol-4-yl)pyridine and Related Ligands: Magnetic, Spectral and Structural Studies. *Aust. J. Chem.* **1986**, *39*, 209–220.

(52) Roberts, T. D.; Little, M. A.; Kershaw Cook, L. J.; Barrett, S. A.; Tuna, F.; Halcrow, M. A. Iron(II) Complexes of 2,6-Di(1-alkylpyrazol-3-yl)pyridine Derivatives – the Influence of Distal Substituents on the Spin State of the Iron Center. *Polyhedron* **2013**, *64*, 4–12.

(53) Capel Berdiell, I.; Kulmaczewski, R.; Halcrow, M. A. Iron(II) Complexes of 2,4-Dipyrazolyl-1,3,5-triazine Derivatives – the Influence of Ligand Geometry on Metal Ion Spin state. *Inorg. Chem.* **2017**, *56*, 8817−8828.

(54) Kulmaczewski, R.; Howard, M. J.; Halcrow, M. A. Influence of Ligand Substituent Conformation on the Spin State of an Iron(II)/Di(pyrazol-1-yl)pyridine Complex. *Dalton Trans.* **2021**, *50*, 3464−3467.

(55) Shahid, N.; Burrows, K. E.; Howard, M. J.; Pask, C. M.; Cespedes, O.; McGowan, P. C.; Halcrow, M. A. The Spin States of Diastereomeric Iron(II) Complexes of 2,6-Bis(thiazolin-2-yl)pyridine (ThioPyBox) Ligands, and a Comparison with the Corresponding PyBox Derivatives. *Inorg. Chem.* **2021**, doi: 10.1021/acs.inorgchem.1c01988

(56) (a) Houghton, B. J.; Deeth, R. J. Spin-State Energetics of Fe^{II} Complexes − The Continuing Voyage Through the Density Functional Minefield. *Eur. J. Inorg. Chem.* **2014**, *2014*, 4573−4580. (b) Mortensen, S. R.; Kepp, K. P. Spin Propensities of Octahedral Complexes from Density Functional Theory. *J. Phys. Chem. A* **2015**, *119*, 4041−4050. (c) Siig, O. S.; Kepp, K. P. Iron(II) and Iron(III) Spin Crossover: Toward an Optimal Density Functional. *J. Phys. Chem. A* **2018**, *122*, 4208−4217.

(57) The free ligand DFT calculations confirm the $L^{3'}$ tautomer is lower energy than L^3 in the gas phase (Chart 2, Table S21). That is consistent with previous observations that the *N*2-H tautomer is favored in *C*-substituted 1,2,3-triazoles.[70] However, both spin states of $[Fe(L^3)_2]^{2+}$ have lower energy than $[Fe(L^{3'})_2]^{2+}$, as observed crystallographically (Table 2). Hence, metal chelation changes the tautomeric structure of L^3.

(58) Ashley, D. C.; Jakubikova, E. Ironing Out the Photochemical and Spin-Crossover Behavior of Fe(II) Coordination Compounds with Computational Chemistry. *Coord. Chem. Rev.* **2017**, *337*, 97–111

(59) (a) Reiher, M.; Salomon, O.; Hess, B. A. Reparameterization of Hybrid Functionals Based on Energy Differences of States of Different Multiplicity. *Theor. Chem. Acc.* **2001**, *107*, 48−55. (b) Zein, S.; Borshch, S. A.; Fleurat-Lessard, P.; Casida, M. E.; Chermette, H. Assessment of the Exchange-Correlation Functionals for the Physical Description of Spin Transition Phenomena by Density Functional Theory Methods: All the Same? *J. Chem. Phys.* **2007**, *126*, 014105.

(60) For example, the aqueous basic pK_a is 1.2 for 1-methyl-1,2,3-triazole; 2.9 for 4{5}-methyl-1,2,3-triazole, and −3.5 for 2-methyl-1,2,3-triazole.[71] While these pK_as vary between solvents, the trends between the compounds are retained in each case. Lõkov, M.; Tshepelevitsh, S.; Heering, A.; Plieger, P.; Vianello, R.; Leito, I. On the Basicity of Conjugated Nitrogen Heterocycles in Different Media. *Eur. J. Org. Chem.* **2017**, *2017*, 4475–4489.

(61) Halcrow, M. A.; Capel Berdiell, I.; Pask, C. M.; Kulmaczewski, R. Relationship between the Molecular Structure and Switching Temperature in a Library of Spin-Crossover Molecular Materials. *Inorg. Chem.* **2019**, *58*, 9811–9821.

(62) McPherson, J. N.; Elton, T. E.; Colbran, S. B, A Strain-Deformation Nexus within Pincer Ligands: Application to the Spin States of Iron(II) Complexes. *Inorg. Chem.* **2018**, *57*, 12312–12322.

(63) See *eg* (a) Kim, Y.; Kim, S.-J.; Lough, A. J. New Dirhodium(II, II) Carboxylates with 2,6-Bis(*N*'-1,2,4-triazolyl)pyridinato Ligand (btp). *Polyhedron* **2001**, *20*, 3073−3078. (b) Hong, S. J.; Ryu, J. Y.; Lee, J. Y.; Kim, C.; Kim, S.-J.; Kim, Y. Synthesis, Structure and Heterogeneous Catalytic Activities of Cu-Containing Polymeric Compounds: Anion Effect and Comparison of Homogeneous vs. Heterogeneous Catalytic Activity. *Dalton Trans.* **2004**, *2004*, 2697−2701. (c) Ryu, J. Y.; Lee, J. Y.; Choi, S. H.; Hong, S. J.; Kim, C.; Kim, Y.; Kim, S.-J. Syntheses and Structures of Ag(I) Compounds Containing btp Ligands *Inorg. Chim. Acta* **2005**, *358*, 3398−3406. (d) Ryu, J. Y.; Han, J. H.; Lee, J. Y.; Hong, S. J.; Choi, S. H.; Kim, C.; Kim, S.-J.; Kim, Y. Crystal Structures and Catalytic Activities of Zn(II) Compounds Containing btp Ligands. *Inorg. Chim. Acta* **2005**, *358*, 3659−3670. (e) K.-T. Youm, J. Ko and M.-J. Jun, Polyhedron, 2006, 25, 2318; Youm, K.-T.; Woo, H. K.; Ko, J.; Jun, M.-J. Multiple-decked Gd(III) Complexes Induced by Hydrogen Bonds Depending on Anions. *CrystEngComm* **2007**, *9*, 30−34. (f) Shi, Y.-J.; Chen, L.-L.; Liu, Y.; Wu, Y.-Y.; Li, Y.-M.; Dang, D.-B.; Bai, Y. Isopolymolybdate-Based Cobalt/Nickel Coordination Polymers Constructed by V-Type N-Donor Ligands. *Inorg. Chem.* **2021**, *60*, 1264−1273.

(64) Kim, Y.; Huh, S. Pore Engineering of Metal–Organic Frameworks: Introduction of Chemically Accessible Lewis Basic Sites Inside MOF Channels. *CrystEngComm* **2016**, *18*, 3524−3550.

(65) For example, the aqueous basic pK_a is 2.5 for 1-methylpyrazole, and 3.3 for 3{5}-methyl-1*H*-pyrazole.[71] These values are more similar to each other, than for the different isomers of methyl-1,2,3-triazole.[60]

(66) (a) Capel Berdiell, I.; Kulmaczewski, R.; Cespedes, O.; Halcrow, M. A. An Incomplete Spin-Transition Associated with a Z' = 1 → Z' = 24 Crystallographic Symmetry Breaking. *Chem. Eur. J.* **2018**, *24*, 5055–5059. (b) García-López, V.; Palacios-Corella, M.; Cardona-Serra, S.; Clemente-León, M.; Coronado, E. Spin-Crossover Iron(II) Complex Showing Thermal Hysteresis Around Room Temperature with Symmetry Breaking and an Unusually High *T*(LIESST) of 120 K *Chem. Commun.* **2019**, *55*, 12227–12230. (c) Al-Azzani, M. A.; Al-Mjeni, F.; Mitsuhashi, R.; Mikuriya, M.; Al-Omari, I. A.; Robertson, C. C.; Bill, E.; Shongwe, M. S. Unusual Magneto-Structural Features of the Halo-Substituted Materials $[Fe^{III}(5\text{-X-salMeen})_2]Y$: a Cooperative [HS-HS]↔[HS-LS] Spin Transition. *Chem. Eur. J.* **2020**, *26*, 4766–4779.

(67) Recent reports of complete SCO involving symmetry-breaking phase transitions: (a) Kulmaczewski, R.; Cespedes, O.; Halcrow, M. A. Gradual Thermal Spin-Crossover Mediated by a Reentrant *Z*' = 1 → *Z*' = 6 → *Z*' = 1 Phase Transition. *Inorg. Chem.* **2017**, *56*, 3144−3148. (b) Phonsri, W.; Davies, C. G.; Jameson, G. N. L.; Moubaraki, B.; Ward, J. S.; Kruger, P. E.; Chastanet, G.; Murray, K. S. Symmetry Breaking Above Room Temperature in an Fe(II) spin Crossover Complex with an N_4O_2 Donor Set. *Chem. Commun.* **2017**, *53*, 1374−1377. (c) Zhang, D.; Trzop, E.; Valverde-Muñoz, F. J.; Piñeiro-López, L.; Muñoz, M. C.; Collet, E.; Real, J. A. Competing Phases Involving Spin-State and Ligand Structural Orderings in a Multistable Two-Dimensional Spin Crossover Coordination Polymer. *Cryst. Growth Des.* **2017**, *17*, 2736−2745. (d) Rosario-Amorin, D.; Dechambenoit, P.; Bentaleb, A.; Rouzières, M.; Mathonière, C.; Clérac, R. Multistability at Room Temperature in a Bent-Shaped Spin-Crossover Complex Decorated with Long Alkyl Chains. *J. Am. Chem. Soc.* **2018**, *140*, 98−101. (e) Hang, H.; Fei, B.; Chen, X. Q.; Tong, M. L.; Ksenofontov, V.; Gural'skiy, I. A.; Bao, X. Multiple Spin Phases in a Switchable Fe(II) Complex: Polymorphism and Symmetry Breaking Effects. *J. Mater. Chem. C* **2018**, *6*, 3352−3361. (f) Fürmeyer, F.; Carrella, L. M.; Ksenofontov, V.; Möller, A.; Rentschler, E. Phase Trapping in Multistep Spin Crossover Compound. *Inorg. Chem.* **2020**, *59*, 2843−2852. (g) Hagiwara, H.; Minoura, R.; Udagawa, T.; Mibu, K.; Okabayashi, J. Alternative Route Triggering Multistep Spin Crossover with Hysteresis in an Iron(II) Family Mediated by Flexible Anion Ordering. *Inorg. Chem.* **2020**, *59*, 9866−9880. (h) Kobayashi, F.; Komatsumaru, Y.; Akiyoshi, R.; Nakamura, M.; Zhang, Y.; Lindoy, L. F.; Hayami, S. Water Molecule-Induced Reversible Magnetic Switching in a Bis-Terpyridine Cobalt(II) Complex Exhibiting Coexistence of SpinCrossover and Orbital Transition Behaviors. *Inorg. Chem.* **2020**, *59*, 16843−16852.

(68) Guionneau, P.; Marchivie, M.; Bravic, G.; Létard, J.-F.; Chasseau, D. Structural Aspects of Spin Crossover. Example of the $[Fe^{II}L_n(NCS)_2]$ Complexes. *Top. Curr. Chem.* **2004**, *234*, 97−128.

(69) McCusker, J. K.; Rheingold, A. L.; Hendrickson, D. N. Variable-Temperature Studies of Laser-Initiated $^5T_2$-$^1A_1$ Intersystem Crossing in Spin-Crossover Complexes: Empirical Correlations between Activation Parameters and Ligand Structure in a Series of Polypyridyl Ferrous Complexes. *Inorg. Chem.* **1996**, *35*, 2100−2112.

(70) (a) Abboud, J.-L. M.; Foces-Foces, C.; Notario, R.; Trifonov, R. E.; Volovodenko, A. P.; Ostrovskii, V. A.; Alkorta, I.; Elguero, J. Basicity of *N*-H- and *N*-Methyl-1,2,3-triazoles in the Gas Phase, in Solution, and in the Solid State − An Experimental and Theoretical Study. *Eur. J. Org. Chem.* **2001**, *2001*, 3013−3024. (b) Oziminskia, W. P.; Dobrowolski, J. C.; Mazurek, A. P. DFT Studies on Tautomerism of C5-Substituted 1,2,3-Triazoles. *J. Mol. Struct.* **2003**, *651–653*, 697–

704. (c) Ramírez, M. A.; Martín, V. S.; Gallardo, A. C. Studies on Tautomeric Stability and Equilibrium of 5(4)-Substituted-1,2,3-Triazoles. I. Electronegativity and Resonance Effects of Substituent. *Comput. Theor. Chem.* **2013**, *1026*, 31–37.

(71) Catalan, J.; Abboud, J. L. M.; Elguero, J. Basicity and Acidity of Azoles. *Adv. Heterocycl. Chem.* **1987**, *41*, 187−274.